Structure-property relationships of recycled lithium-ion battery cathodes: Microstructure optimization using virtual materials testing

Lukas Fuchs[1,*], Philipp Rieder[1,*], Donal P. Finegan[2], Francois Usseglio-Viretta[2], Jeffrey Allen[2], Melissa Popeil[3], Orkun Furat[1,4], Volker Schmidt[1]

January 29, 2026

[1]Institute of Stochastics, Ulm University, Helmholtzstraße 18, D-89069 Ulm, Germany

[2]National Laboratory of the Rockies, 15013 Denver W Parkway, Golden, CO 80401, USA

[3]Mines/NLR Advanced Energy Systems Graduate Program, Colorado School of Mines, Golden, Colorado, 80401 USA

[4]SDU Applied AI and Data Science Unit, University of Southern Denmark, Campusvej 55, DK-5230 Odense, Denmark

*Corresponding authors. lukas.fuchs@uni-ulm.de, philipp.rieder@uni-ulm.de;

LF and PR contributed equally to this paper.

Keywords:

Virtual materials testing; pristine NMC; recycled NMC; end-of-life NMC; stochastic modeling; virtual microstructure generation; Li-ion battery;

Abstract

The increasing demand for sustainable battery technologies requires effective recycling strategies for end-of-life lithium-ion battery cathodes. In this study, virtual materials testing, a well-established framework for modeling conventionally manufactured NMC-based cathodes, is applied to partially recycled cathodes. To this end, virtual cathodes consisting of mixtures of pristine and recycled NMC particles are utilized to systematically analyze structure-property relationships in dependence of mixing ratios and different spatial arrangement strategies. For this purpose a stochastic 3D model is developed that is capable of generating virtual cathodes with arbitrary volume fractions of active materi-

als, and mixing ratios of pristine and recycled NMC particles. Particularly, the stochastic 3D model can mimic the different size distributions of pristine and recycled particles that are observed in image data. Additionally, the model allows the structuring of pristine and recycled NMC either uniformly mixed or layer-wise arranged. Subsequently, a systematic computational analysis is conducted to assess the influence of increasing active material ratios of recycled particles, ranging from 0 % to 100 %, while maintaining a constant overall active material volume fraction. The impact of particle mixing on cathode performance is evaluated by examining transport-relevant geometrical descriptors and effective properties, such as geodesic tortuosity, specific surface area, and tortuosity factor.

1 Introduction

The rapid growth in demand for electric vehicles (EVs) and energy storage systems has driven an unprecedented increase in battery production, with global EV battery output projected to reach 3 TWh by 2030 [1]. Especially, lithium-ion batteries are widely used due to their high energy density accounted for about 60% of EV battery capacity in 2022 [2, 3]. However, their popularity results in an increasing demand for raw materials, which poses several challenges, including the need to scale in the mining industry and geopolitical concerns associated with the concentration of these materials. This is especially critical for materials such as lithium and cobalt [4, 5].

As battery manufacturing accelerates, managing end-of-life (EOL) lithium-ion batteries becomes critical. By 2030, EV batteries with a cumulative storage capacity of 100–120 GWh are expected to reach EOL [6], corresponding to approximately 1.2 million metric tons of material from batteries of electric vehicles alone [7]. Additionally, the European Union plans to introduce mandatory recycling quotas for lithium-ion batteries by 2031, requiring new batteries to consist of at least 6 % recycled lithium, 6 % recycled nickel, and 16 % recycled cobalt [8]. These two developments, large volumes of EOL batteries and upcoming recycling requirements, necessitates the development of sustainable recycling technologies to address both limitations in new materials and environmental concerns of the disposal of end-of-life batteries [9].

Current battery recycling approaches can be categorized into three main processes: pyrometallic, hydrometallurgical, and direct recycling methods [10]. In pyrometallurgical processes, high-temperature melting is utilized to extract and recover the active materials of lithium-ion batteries, offering, among other benefits, a relatively simple operation and comparatively low environmental impacts [11]. Nevertheless, a major drawback of pyrometallurgical processes is their high energy demand [12]. Hydrometallurgical methods rely on chemical leaching to dissolve valuable metals from end-of-life batteries, generally achieving higher recovery rates than pyrometallurgical processes. However, they also generate significant amounts of chemical waste [11, 13]. Non destructive direct recycling aims

to recycle not only specific or valuable elements but also to recover complete battery components, such as current collectors and electrode materials, binder and electrolyte. These components undergo purification, cleaning and optional regeneration processes before being reused in new batteries [14]. Direct recycling, while potentially the most sustainable approach, faces challenges in maintaining desired structural and electrochemical properties of recovered materials [15]. Recent studies have further highlighted the influence of micostructural damage of $LiNi_xMn_yCo_zO_2$ (NMCxyz, hereafter referred to as NMC) cathode particles in Li-ion batteries, such as severe cracks in active materials in cathode recycling [16].

The performance of battery cathodes, such as Li-ion cathodes, is determined in parts by microstructural features, e.g., the size and shape distribution of active particles and their spatial arrangement within the electrodes. For example, Li-ion transport and charge reactions depend on geometric factors like porosity, pore connectivity (tortuosity), interfacial area, and particle arrangement. In literature, the relationship between microstructure and effective properties in porous electrode materials has been extensively studied using both experimental and computational approaches [3]. Advanced characterization techniques, including X-ray computed tomography and focused ion beam scanning electron microscopy, have enabled detailed three-dimensional visualization of electrode microstructures [17, 18]. These 3D images enable computational analyses; for example, volume fractions, specific surface areas, mean chord lengths, and tortuosities directly from tomographic image stacks. Such metrics have been shown to strongly correlate with effective transport properties, e.g. high tortuosity or bottle neck effects slow ion diffusion [19–21]. Complementary numerical modeling approaches have further advanced the understanding through simulations that connect microstructural features to electrochemical performance [22–25].

Previously mentioned computational modeling approaches have primarily focused on pristine cathode materials, establishing fundamental structure-property relationships for cathodes derived from measured image data [3, 26–28]. In most of these studies, the analysis concentrates on the geometry of the active material phase, while neglecting the carbon–binder domain (CBD) for simplicity. This simplification is justified, as the active material particle arrangement largely determines the pore network through which lithium ions diffuse, whereas the CBD occupies a comparatively small volume and primarily provides electronic conductivity and mechanical integrity.

Building on these foundations, recent advances in virtual materials testing have proven their large potential by integrating stochastic microstructure models [29, 30] for virtual material generation with tools for predicting transport properties [23]. However, cycled cathode materials often exhibit fundamentally different microstructural features compared to their pristine counterparts, including altered primary particle morphology and the existence of cracks [31–33]. Moreover, the incorporation of recycled materials into mixed

cathode systems introduces additional complexity, which has not yet been systematically investigated. For instance, uniformly mixing recycled and new particles could lead to different pore space morphologies than segregating them in layers. In analogous contexts, graded or layered electrode designs are known to influence performance. While grading has been studied for optimizing electrodes [34], the impact of integrating recycled materials on the microstructure and resulting effective properties has not yet been systematically explored. In particular, the spatial distribution of recycled versus pristine particles represents a critical design parameter influencing electrode performance. Uniformly mixed and layered cathodes show very distinct pore architectures and transport pathways.

This work introduces a 3D model for the stochastic generation of uniformly mixed and layered virtual cathodes, consisting of varying ratios of pristine and recycled NMC particles. The model comprises two components: the stochastic 3D model for generating pristine particles described in [30], which has been calibrated to experimentally measured data as well as a stochastic 3D model for the EOL phase which is calibrated to 3D CT images in this paper. Note that pristine and recycled particles follow different size distributions, as the smaller recycled particles are assumed to have undergone direct recycling processes, in which secondary particles break down into clusters of, or even individual, primary particles. Further, it is assumed that pristine and recycled particles differ only in their morphology, while being similar in their chemical and electrochemical properties.

This study aims to establish quantitative structure-property relationships for virtual cathode microstructures exhibiting different mixing ratios of active materials. The primary objectives are: (1) to develop a computational framework for generating realistic mixed pristine-recycled cathode microstructures with controlled spatial arrangements, (2) to quantify the impact of the ratio of recycled active material and arrangement strategy on key transport properties, and (3) to identify optimal integration strategies that maintain cathode performance while maximizing the recycling active material fraction.

The novelty of this work lies in the systematic computational approach to mixed material microstructure generation and the analysis of geometric and transport descriptors as functions of recycled content and its spatial distribution, providing guidelines for sustainable battery manufacturing.

2 Materials and Methods

The focus of this section is on the generation of virtual mixed cathodes, consisting of pristine and recycled active material particles consisting of $LiNi_xMn_yCo_zO_2$ (NMCxyz). In the context of the present paper, a cathode is characterized by its active material phase and pore space. First, in Section 2.1 virtual pristine NMC811 particles are generated utilizing the stochastic microstructure model introduced in [30]. These particles are

subsequently packed to represent a pristine cathode.

In Section 2.2, a virtual cathode consisting of recycled active material is generated by means of a marked tessellation, i.e., a partition of the three-dimensional space into disjoint subsets, each assigned a scalar-valued mark. The so-called cells of this tessellation mimic fragments of recycled NMC111, which have been fractured as a result of cycling and chemical treatments during the recycling process.

These two virtual cathodes are combined in Section 2.3 by iteratively removing pristine particles from the pristine cathode and replacing them with recycled particle (RP) fragments. This replacement is performed according to two different structuring scenarios occurring in real world cathode manufacturing [34], enabling either a uniform or layered distribution of RP fragments within the virtual cathode, while keeping the overall active material volume fraction constant.

Lastly, in Section 2.4, several microstructure descriptors are introduced, which are used in Section 3 for a statistical analysis of the geometry and effective properties of differently structured mixed cathodes.

2.1 Pristine NMC811 particles

The pristine particles considered in this work are generated by the stochastic microstructure model introduced in a previous study [30]. There, the 3D microstructure of a pristine NMC811 cathode was imaged using X-ray nano-computed tomography, and individual particles have been segmented. To statistically capture the observed particle shapes, a stochastic 3D model based on random fields on the sphere has been fitted to the segmented image data. Specifically, particle surfaces were stochastically modeled using a series expansion with random coefficients, which implicitly model both particle size and shape distribution. The stochastic 3D model enables the generation of synthetic particle surfaces that are statistically consistent with the experimental observations. In [30], a high degree of agreement between the model realizations and the measured particle geometries was observed.

In the present work, particles generated by this model are packed into a virtual cathode, following the approach described in [35]. More precisely, in a first step, a certain number of volume-equivalent placeholder spheres are randomly positioned in a cubic sampling window. To eliminate the overlaps between the spheres, a force-biased algorithm [36, 37] is applied. Finally, each sphere is replaced by its corresponding NMC particle counterpart, i.e., by a virtual particle generated by the stochastic 3D model.

More formally, let $P_1, P_2, \ldots$ be a sequence of independent realizations of the particle model described in [30], where $P_i = \{x \in \mathbb{R}^3 \colon x \text{ belongs to the } i\text{-th particle}\} \subset \mathbb{R}^3$ denotes a particle, whose barycenter is aligned with the origin of the coordinate system. Let $W = [0, 250)^3 \subset \mathbb{R}^3$ denote a cubic, unitless sampling window. In the present work W

corresponds to a cubic observation window of side length of $250 \cdot 128\,\mathrm{nm}$=32 µm. Further, let $n \in \mathbb{N} = \{1, 2, 3, \ldots\}$ denote the number of particles to be placed within W. The value of n is determined as

$$n = \max\left\{ i \in \mathbb{N} \colon \frac{\sum_{j=1}^{i} \nu_3(P_j)}{\nu_3(W)} \leq \varepsilon_{\max} \right\},$$

where $\nu_3(P_j)$ denotes the volume of $P_j \subset \mathbb{R}^3$ and $\varepsilon_{\max} \in [0, 1]$ the desired maximum active material volume fraction. In the present work, $\varepsilon_{\max} = 0.65$ is set.

For each particle P_j, let $S_j \subset \mathbb{R}^3$ denote a corresponding volume-equivalent placeholder sphere, i.e., $\nu_3(P_j) = \nu_3(S_j)$. To initialize the packing, uniformly distributed points $c'_1, \ldots, c'_n \in W$ are used as initial centers of the placeholder spheres.

The spheres are then packed, under periodic boundary conditions, minimizing their mutual overlap within W utilizing a force-biased algorithm [36, 37]. That is, the spheres are iteratively moved according to repulsive forces proportional to their overlap with neighboring spheres. Consequently, an overlap-free sphere remains at its position unless it is displaced in subsequent iterations by interactions with moving neighbors.

This procedure yields new center points $c_1, \ldots, c_n \in W$, resulting in a packed placeholder sphere system $\cup_{i=1}^{n}(S_i + c_i)$, where $S_i + c_i = \{s + c_i \text{ for all } s \in S_i\}$. An exemplary cross section of a packed sphere system is shown in Figure 1(a).

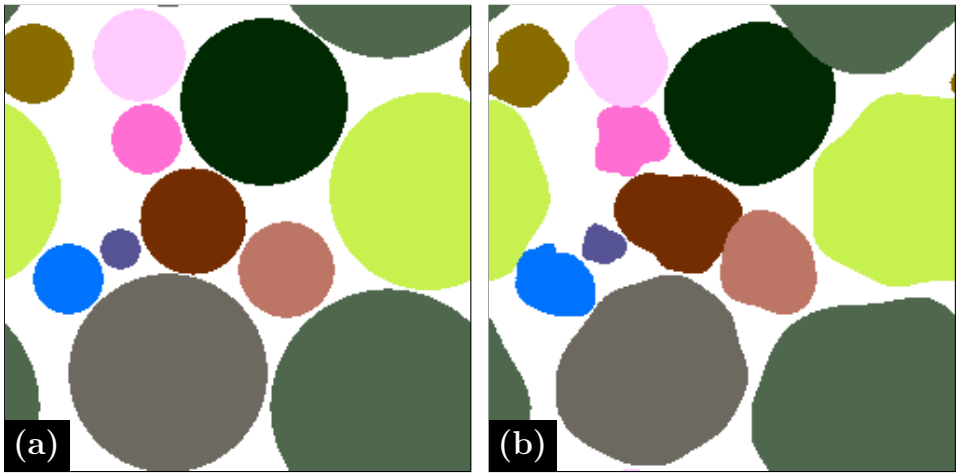

Figure 1: Placeholder spheres packed with minimal overlap within the sampling window (a). Subsequently, these spheres are replaced by volume-equivalent particles by aligning their barycenters with the centers of the respective sphere (b). Each individual sphere and its corresponding particle are shown in false colors for visualization purposes, i.e., the colors have no physical meaning.

Subsequently, the placeholder spheres $S_1, \ldots, S_n$ are replaced by the corresponding virtual pristine NMC particles $P_1, \ldots, P_n$, which are positioned at their respective center

points $c_1, \ldots, c_n \in W$. Formally, this replacement yields a particle system, given by

$$\mathcal{P}_n = \cup_{i=1}^{n}(P_i + c_i), \tag{1}$$

which will hereafter be referred to as the particle phase. Further, the particle phase can be considered as a virtual cathode, consisting of pristine NMC particles. A visualization of the particle phase is presented in Figure 1(b).

Note that this replacement procedure may introduce new overlaps or remove existing ones, thereby decreasing or increasing the actual active material volume fraction ε, which is defined as

$$\varepsilon(\mathcal{P}_n) = \frac{\nu_3(\mathcal{P}_n)}{\nu_3(W)}.$$

The resulting particle phase is rejected whenever ε falls below a predefined threshold $\varepsilon_{\min} \in [0, \varepsilon_{\max})$ or exceeds the maximum allowed active material fraction $\varepsilon_{\max}$. In this work $\varepsilon_{\min} = 0.62$, which ensures that the resulting active material volume fraction satisfies $0.62 \leq \varepsilon \leq 0.65 = \varepsilon_{\max}$. In the case of rejection, the modeling procedure is repeated with new particle realizations $P_1', P_2', \ldots$. This simulation strategy is well-known in literature as "rejection sampling" or "acceptance-rejection method" [38].

Recall that the particles are packed using periodic boundary conditions. However, from now on, we consider the particle system under non-periodic boundary conditions. Consequently, only the representative in W of each particle is considered, and any particle that is split into multiple disconnected components is relabeled so that each connected component of $\mathcal{P}_n$ receives a unique label. This results in $\tilde{n} \geq n$ labeled connected components. Note that this also influences the number and position of the barycenters of the particles. For simplicity, each connected component is hereafter referred to as a "particle", and the notation n is used instead of $\tilde{n}$. Accordingly, the particle phase is denoted by $\mathcal{P}_n = \cup_{i=1}^{n}(P_i + c_i)$ with particles $P_1, \ldots, P_n$ centered at $c_1, \ldots, c_n$.

2.2 Recycled NMC111 particles

As a basis for the RP fragment model, a cathode consisting of recycled particles was manufactured experimentally.

To obtain recycled particle (RP) fragments, a commercial large-format pouch cell with a capacity of 64 Ah consisting of a NMC111 cathode, a graphite anode, and a carbonate electrolyte was cycled to EOL. The cell was charged and discharged at 30° with a 1.8 C rate to 80% depth of discharge and a 50% duty cycle, as described in [16]. After cycling, the cathode sheets were removed from the spent pouch cell and cut into small pieces. The NMC particles were removed from the current collector utilizing a solution process at Oak Ridge National Lab, similar to the approach described in [39], employing a 0.1

M KH_2PO_4 buffer solution with an added volume of Triton^{TM} X-100 surfactant. The recovered particles were then dried and stored as powder.

Subsequently, a cathode was manufactured from these RP fragments, containing 4 wt% conductive carbon, 4 wt% PVDF binder, and 92 wt% RP fragments serving as cathode active material. The slurry was dried and calendared to a coating thickness of 50 µm, yielding a loading of approximately 1.5 mAh/cm^2.

To asses the microstructure of this cathode X-ray nano-CT images were acquired using a Zeiss Ultra 810 system. A binning factor of 2 was applied to achieve a voxel size of 128 nm, matching the resolution used for the generation of the pristine particles in Section 2.1. The radiographs for the CT reconstructions were obtained in phase contrast mode using the large-field-of-view setting, where the field of view was 64 µm × 64 µm. Figure 2(a) shows a cross-section of the resulting 3D image, where the RP fragments appear brighter, while the pore space is darker. As with pristine NMC particles, the RP fragments retain a polycrystalline structure. However, they are generally not spherical, and some fragments have broken down into individual crystals.

Note that the image data of the RP fragment phase, shown in Figure 2(a), does not allow for a straight-forward 3D segmentation of individual RP fragments, due to insufficient resolution. Consequently, a subsequent virtual packing of fragments, similar to the procedure described in Section 2.1 for pristine particles, is not feasible. Moreover, a phase-wise segmentation based on simple (local) thresholding does not yield satisfactory results because of the noise present in the image data. To overcome these limitations, a different approach based on a marked tessellation is utilized to model the RP fragment phase. Instead of identifying individual particles, a two-phase representation is employed, distinguishing only between the pore space and the RP fragment phase. For this purpose, the gray scale image data is first approximated by a marked Voronoi tessellation-based representation [40]. A Voronoi tessellation is a low-parametric mathematical concept that is widely used to effectively represent polycrystalline materials and, consequently, the inner grain architecture of NMC particles [31, 41–43]. To mimic a grayscale image, each Voronoi cell is assigned a scalar value representing its grayscale level. To obtain a phase-wise segmentation, the marks of the tessellation are thresholded such that certain cells represent RP fragments, while the remaining cells correspond to the pore space, resulting in a two-phase representation of the virtual cathode. This approach reduces both the noise in the image data as well as the dimensionality and complexity of the measured microstructure.

Formally, the modeling procedure is defined as follows. The marked Voronoi tessellation is given by a set of tuples $\mathcal{T} = \{(s_i, t_i) \colon i = 1, \dots, m\}$, where each tuple $(s_i, t_i) \in \mathbb{R}^3 \times [0, 1]$ consists of a so-called seed point s_i and an associated mark t_i. The set $\mathcal{T}$ induces a partition of the observation window W into pairwise internally disjoint

sets $C_1, \ldots, C_n \subset \mathbb{R}^3$, often referred to as cells, where

$$C_i = \{x \in W : |x - s_i| \leq |x - s_j| \text{ for all } j = 1, \ldots, m\}.$$

Thereby, $|\cdot|\colon \mathbb{R}^3 \to [0, \infty)$ denotes the Euclidean norm. Note that the cells C_i for $i = 1, \ldots, m$ exhibit piecewise planar boundaries, a frequently observed characteristic of NMC grains [42]. Furthermore, the marked tessellation $\mathcal{T}$ implicitly assigns the mark t_i to each point within C_i. To generate an adequate representation of a cathode consisting of RP fragments, the parameters (s_i, t_i) for $i = 1, \ldots, m$ are fitted to the image data.

To do so, the seed points and marks are optimized such that the resulting tessellation resembles a 3D gray scale image of a cathode $Z\colon \{1, \ldots, 250\}^3 \to [0, 1]$. Thereby, a cell C_i of the tessellation contains voxels of relatively homogeneous gray scale values $Z(x)$. The corresponding mark t_i can be interpreted as the representative gray scale value of the voxels $x \in C_i \cap \{1, \ldots, 250\}^3$. Thereby, the optimization aims to minimize the discrepancy between t_i and the mean grayscale value of all voxels in $C_i \cap \{1, \ldots, 250\}^3$ for all $i = 1, \ldots, m$.

Mathematically, the minimization problem states

$$\mathcal{T}^* = \underset{\mathcal{T} \in \mathbb{T}}{\operatorname{argmin}} \sum_{x \in \{1,\ldots,250\}^3} \left(\sum_{i=1}^{m} \frac{t_i \exp(-|x - s_i|)}{\sum_{j=1}^{m} \exp(-|x - s_j|)} - Z(x) \right)^2, \tag{2}$$

where $\mathbb{T}$ denotes the space of tessellations.

Intuitively speaking, the expression within the outer parenthesis quantifies the discrepancy between the mark t_i at a voxel $x \in C_i \cap \{1, \ldots, 250\}^3$ and its actual gray scale value $Z(x)$, whereas the outer sum accumulates these discrepancies over the entire voxel grid. The exponential terms in the fraction ensure differentiability, allowing the use of gradient descent-based optimization schemes to solve the minimization problem. For further details on Eq. (2), the reader is referred to [30, 44].

For this purpose, initially, $m = 60\,000$ tuples (s_i, t_i) are sampled uniformly and independently within the domain $W \times [0, 1]$, forming the initial marked tessellation $\mathcal{T}$. The minimization problem in Eq. (2) is then numerically solved using the Adam optimizer [45] with a learning rate of 0.3. The number of cells, $m = 60\,000$, was chosen heuristically to balance the preservation of granular features observed in the CT image Z with a relatively low cell/ parameter count. This choice allows for substantial dimensionality reduction (reducing the number of parameters by a factor of $60\,000 \cdot 4/250^3 \approx 0.015$), improves computational efficiency, and effectively suppresses noise.

Figure 2(b) shows an exemplary cross section of the fitted tessellation $\mathcal{T}^*$, where each displayed voxel is colored by its corresponding mark. The tessellation-based parametric representation inherently suppresses noise in the raw data by grouping spatially close voxels with similar gray scale values into homogeneous regions, i.e., cells. Note that there

is a high similarity between this procedure and k-means clustering [46] and super-pixel clustering [47].

To obtain a two-phase representation distinguishing between the RP fragment phase and pore space, a threshold $t \in [0,1]$ is applied to the marks $t_1, \ldots, t_m$ to determine whether the corresponding cells $C_1, \ldots, C_m$ belong to the RP fragment phase. More precisely, the RP fragment phase $\mathcal{E}(t) \subset W$ based on the fitted marked tessellation $\mathcal{T}^*$ is given by

$$\mathcal{E}(t) = \bigcup_{i \in I} C_i,$$

where $I = \{i \colon t_i \geq t \text{ for } i = 1, \ldots, m\}$.

Note that $\mathcal{E}(t)$ preserves key structural features of both the tessellation and the original 3D grayscale image, such as the granular structure and the piecewise-planar boundaries. For a suitable $t \in [0,1]$, $\mathcal{E}(t)$ can be considered a virtual cathode consisting of RP fragments. Moreover, this unsupervised approach does not require manual segmentation and avoids several limitations of conventional segmentation techniques. For example, classical thresholding methods [48] are highly sensitive to image noise and may result in pores in RP fragments that contradict model assumptions. More advanced thresholding approaches attempt to address this problem through image smoothing, e.g., by applying Gaussian kernels. However, they tend to produce overly rounded phase interfaces [49]. Similar drawbacks are observed for black-box methods such as neural network- or random forest–based segmentation techniques [50, 51], which additionally require manually annotated training data.

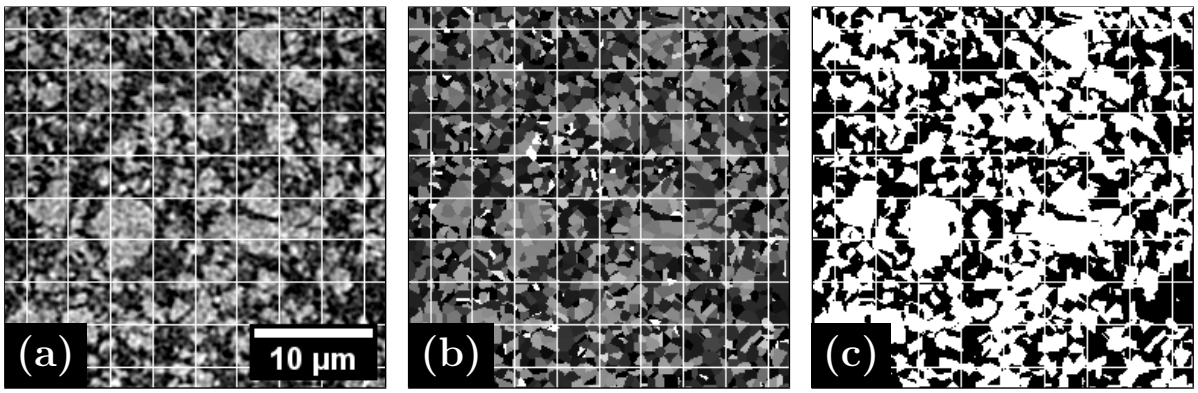

Figure 2: Modeling of RP fragment phase. (a) Cross-section of measured gray scale image. (b) Cross-section of corresponding fitted parametric gray scale image. (c) Visualization of a cross-section of $\mathcal{E}(t)$ for a $t \in [0,1]$ corresponding to (b). Note for comparison purposes a grid was added to each figure.

2.3 Virtual Cathode Generation

The virtual cathode microstructures considered in the present paper are generated by a systematic combination of the pristine particle phase, derived by packing pristine particles (see Section 2.1), and the tessellation-based representation of the RP fragment phase (see Section 2.2). To achieve this, pristine NMC particles are iteratively removed and replaced by RP fragments according to different structuring scenarios. In each iteration, the local active material volume fraction is kept constant, while the mixing ratio of pristine particles and RP fragments is systematically varied, thereby ensuring comparability among the evolving microstructures.

This procedure can be mathematically described as follows. Let $P_1, \ldots, P_n \subset \mathbb{R}^3$ be a sequence of pristine particles, $c_1, \ldots, c_n \in W$ the corresponding positions of their barycenters, and $\mathcal{P}_n$ the pristine particle phase as introduced in Eq. (1). To generate cathodes with varying ratios of pristine particles and RP fragments, a sequence of pristine particle phases with a successively reduced number of pristine particles are defined. To uphold an overall constant volume fraction of the active material phase, any loss of active material by the removal of pristine particles is compensated by filling the microstructure with RP fragments.

For that, let $\mathcal{P}_0, \ldots, \mathcal{P}_n$ be a sequence of pristine particle phases, given by $\mathcal{P}_0 = \emptyset$ and $\mathcal{P}_j = \cup_{i=1}^{j}(P_{(i)} + c_{(i)})$ for $j = 1, \ldots, n$, where $P_{(i)}$ denotes the i-th particle with respect to some ordering, and $c_{(i)}$ the respective barycenter. Note that the particle phases are nested, i.e., $\mathcal{P}_0 \subset \ldots \subset \mathcal{P}_n$. To obtain differently structured active material phases, let the particles $P_1, \ldots, P_n$ be ordered according to one of the following scenarios:

(i) **Uniform:** The sequence $P_{(1)}, \ldots, P_{(n)}$ is derived by a random permutation of the particles $P_1, \ldots, P_n$. Consequently, the obtained particle phases $\mathcal{P}_0, \ldots, \mathcal{P}_{n-1}$ can be considered as spatially homogeneous thinning of $\mathcal{P}_n$.

(ii) **Gradient:** To generate particle phases exhibiting a structural gradient, let the particles $P_{(1)}, \ldots, P_{(n)}$ with barycenters $c_{(1)} = (x_{(1)}, y_{(1)}, z_{(1)})$, $\ldots$, $c_{(n)} = (x_{(n)}, y_{(n)}, z_{(n)})$ be ordered such that $y_{(1)} \leq \ldots \leq y_{(n)}$, where the y-coordinate corresponds to the direction of charge transport. In this case, $\mathcal{P}_j$ is obtained by only considering the j particles whose centers have the smallest y-coordinates. This strategy results in a vertical gradient along the cathode thickness: the upper region of the sampling window W becomes increasingly depleted of pristine particles with increasing j, while the lower region contains only pristine particles with a packing density similar to $\mathcal{P}_n$. Note that the transition between these regions is gradual, as particles are removed in their entirety rather than partially.

To keep the active material volume fraction constant, RP fragments have to be added to $\mathcal{P}_j$. Recall Section 2.2, where the RP fragment phase $\mathcal{E}(t)$ was introduced, depending on some threshold $t \in [0, 1]$, which controls the number of RP fragments in $\mathcal{E}(t)$ and hence its volume fraction $\varepsilon(\mathcal{E}(t))$. To ensure that all observed differences between different virtual

cathodes rely only on the differently structured active material and not on local variations of active material volume fraction, the local volume fraction is kept constant. For that, let the observation window W be partitioned into ten horizontal layers perpendicular to the y-direction, defined as

$$W_i = \{(x, y, z) \in W \colon (i-1) \cdot 25 \leq y < i \cdot 25\} \quad \text{for } i = 1, \ldots, 10.$$

Further, let $\mathcal{E}_i(t) \subset \mathcal{E}(t)$ denote the i-th layer of the RP phase $\mathcal{E}(t)$, containing those RP fragments $C_k, k = 1, \ldots, m$, whose seed point is located in layer W_i. Formally, $\mathcal{E}_i(t)$ is given by

$$\mathcal{E}_i(t) = \bigcup_{k=1}^{m} \big\{C_k \colon t_k \geq t \text{ and } s_k \in W_i\big\} \subset \mathcal{E}(t),$$

where (s_k, t_k) denotes the tuple of seed point s_k and mark t_k inducing the Voronoi cell C_k.

Then, the (combined) active material phases are defined as

$$\mathcal{B}_j(\ell) = \mathcal{P}_j \cup \Big(\bigcup_{i=1}^{10} \mathcal{E}_i(\ell^{(i)}) \Big) \quad \text{for } j = 0, \ldots, n,$$

with the local threshold vector $\ell = (\ell^{(1)}, \ldots, \ell^{(10)}) \in [0,1]^{10}$. Since $\mathcal{P}_j$ is fixed, the active material volume fraction of $\mathcal{B}_j(\ell)$ depends solely on ℓ. To ensure that all active material phases $\mathcal{B}_j(\ell_j)$ for $j = 0, \ldots, n$ exhibit a layer-wise similar active material volume fraction, the threshold ℓ_j is determined as the minimizer

$$\hat{\ell}_j = \operatorname*{argmin}_{\ell \in [0,1]^{10}} \sum_{i=1}^{10} \big| \varepsilon\big(\mathcal{P}_n \cap W_i\big) - \varepsilon\big(\mathcal{B}_j(\ell_j) \cap W_i\big) \big|, \tag{3}$$

i.e., as vector of thresholds that minimizes the deviation in layer-wise volume fractions between $\mathcal{B}_j$ and the reference particle phase $\mathcal{P}_n$, in which no particles are removed. Note that for $j = n$ it holds $\hat{\ell}_n = 0$, where $0 \in \mathbb{R}^{10}$ denotes the ten-dimensional zero-vector. In this case $\mathcal{P}_n = \mathcal{B}_n(\hat{\ell}_n)$ and consequently $\varepsilon_i(\mathcal{P}_n) - \varepsilon_i(\mathcal{B}_n(\hat{\ell}_n)) = 0$ for all layers $i = 1, \ldots, 10$.

Due to computational efficiency, the minimization problem stated in Eq. (3) was solved utilizing a greedy optimization scheme. More precisely, to obtain the threshold vector $\hat{\ell}_j = (\hat{\ell}_j^{(1)}, \ldots, \hat{\ell}_j^{(10)})$, each component $\hat{\ell}_j^{(i)}$ was determined iteratively by assuming the previously computed $\hat{\ell}_j^{(i')}$ as fixed and solving solving the layer-wise minimization problem

$$\hat{\ell}_j^{(i')} = \operatorname*{argmin}_{\ell \in [0,1]} \big| \varepsilon\big(\mathcal{P}_n \cap W_i\big) - \varepsilon\big(\mathcal{B}_j(\ell) \cap W_i\big) \big|,$$

for $i, i' = 1, \ldots, 10$ and $i' < i$. Note that the greedy approach does not necessarily result

in the optimal solution; however, it provides substantial computational benefits in time and memory.

The whole procedure results in a sequence of active material phases $\mathcal{B}_0(\hat{\ell}_0), \ldots, \mathcal{B}_n(\hat{\ell}_n)$ exhibiting a decreasing proportion of RP fragments compared to pristine particles, however showing layer-wise constant active material fractions. The portion of RP fragments compared to pristine particles is quantified by the recycling fractions $\eta_j \in [0, 1]$, given by

$$\eta_j = \frac{\varepsilon(\mathcal{B}_j(\hat{\ell}_j)) - \varepsilon(\mathcal{P}_j)}{\varepsilon(\mathcal{B}_j(\hat{\ell}_j))}.$$

By construction, it holds $\eta_n = 0$ and $\eta_0 = 1$, i.e., $\mathcal{B}_n(\hat{\ell}_n)$ contains only pristine particles, while $\mathcal{B}_0(\hat{\ell}_0)$ consists exclusively of RP fragments.

In Section 3, the influence of the two structuring scenarios, "uniform" and "gradient", and different recycling fractions η on cathode performance-related descriptors is investigated. For this purpose, the active material phase $\mathcal{A}_\eta$ with a specific recycling fraction $\eta \in [0, 1]$ is defined as $\mathcal{A}_\eta = \mathcal{B}_{j^*}(\hat{\ell}_{j^*})$, where the index j^* is chosen as

$$j^* = \operatorname*{argmin}_{j \in \{0,\ldots,n\}} |\eta - \eta_j|.$$

This ensures that the selected active material phase $\mathcal{A}_\eta$ represents the structure whose recycling fraction η_j most closely matches the desired value η.

Exemplary cross sections of active material phases $\mathcal{A}_\eta$, generated using both structuring strategies and corresponding to recycling fractions $\eta \in \{0, 0.2, \ldots, 0.8, 1\}$ are presented in Figure 3.

2.4 Geometric Descriptors and Properties of Microstructures

To analyze the effects of differently structured active material an extensive microstructural characterization of the virtual two-phase cathodes was performed, using well-known geometric descriptors and effective properties [19, 23, 52–54]. These descriptors quantify the geometry of an active material phase $\mathcal{A} \subset W$ and corresponding pore space $\mathcal{A}^{\mathsf{c}} \subset W$, given by the complement of the active material phase. In the following, all descriptors are defined for some phase $A \in \{\mathcal{A}, \mathcal{A}^{\mathsf{c}}\}$. In this work, we focus on descriptors that are known to influence the performances of battery electrodes [55, 56].

Specific surface area: A basic geometric descriptor for two-phase materials, besides the already considered volume fraction $\varepsilon(A)$ of a phase A, is the specific surface area σ. This descriptor quantifies the interface area between $\mathcal{A}$ and $\mathcal{A}^{\mathsf{c}}$ per unit volume, i.e., $\sigma(A)$

is given by

$$\sigma(A) = \frac{\mathcal{H}_2(\partial A \setminus \partial W)}{\nu_3(W)},$$

where ∂ denotes the boundary of a set, $\nu_3(W)$ the volume of the observation window, and $\mathcal{H}_2(\cdot)$ the 2D Hausdorff measure. Since the interface between $\mathcal{A}$ and $\mathcal{A}^c$ is quantified, it holds $\sigma(\mathcal{A}) = \sigma(\mathcal{A}^c)$. Applied to an electrode battery, it is used to scale the current density of the charge transfer reaction that occurs at the interface between the electrolyte and the active material. To compute a numerical estimation of σ, we apply the convolution-based method of [57].

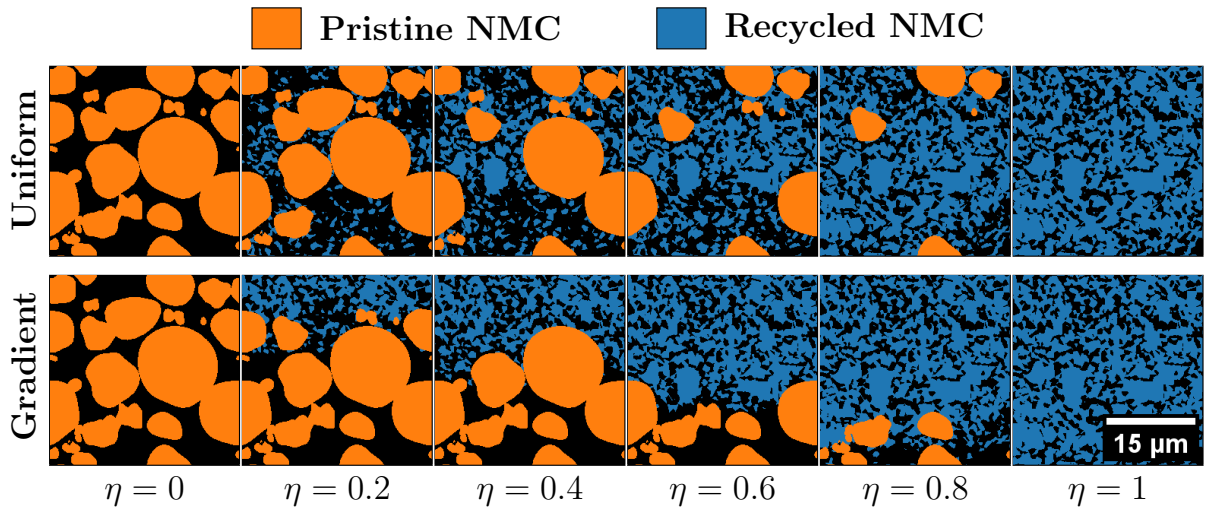

Figure 3: Exemplary cross sections of virtual cathodes $\mathcal{A}_\eta$ generated according to the "uniform" (top row) and "gradient" (bottom row) scenario utilizing a fixed pristine particle phase $\mathcal{P}_n$. The columns show increasing recycling fractions η. The pore space, pristine phase and RP fragment phases are represented in black, orange and blue, respectively. By construction both rows coincide for $\mathcal{A}_0$ and $\mathcal{A}_1$.

Tortuosity factor: The tortuosity factor τ_{fac} is a commonly used measure to describe the diffusivity of porous media [58–60]. It is a key parameter to improve battery performances, especially for fast charging [61]. In this work, it is calculated by using the open-source software TauFactor [23]. TauFactor solves Laplace's equation for steady-state diffusion using a finite difference numerical scheme with Dirichlet-Dirichlet boundary conditions. Because of this, the tortuosity factors calculated here are slightly biased toward lower values, as homogenization calculations are impacted by the choice of the boundary conditions (this dependence eventually vanishes for large enough domains) [62, 63]. The tortuosity factor is given by

$$\tau_{\text{fac}}(A) = \frac{D_0 \cdot \varepsilon(A)}{D_{\text{eff}}} \in [1, \infty)$$

with $D_{\text{eff}} > 0$ being the effective diffusivity in the transport direction (vertical direction in Figure 3), $D_0 > 0$ is the bulk diffusivity of the considered phase and $\varepsilon \in (0, 1)$ the volume fraction of the considered phase. In this work, the bulk conductivity is set to 1 so that the analysis is agnostic with the material property (i.e., D_{eff} is a relative metric). In such a case $D_{\text{eff}} \in [0, 1]$. Note that while τ_{fac} depends on the axis along which transport is considered, it does not take the transport direction into account, unlike the geodesic tortuosity introduced later. A value of $\tau_{\text{fac}} = 1$ corresponds to the ideal case of straight, unobstructed diffusion paths. Larger values of τ_{fac} indicate increasingly tortuous transport paths, i.e., diffusing electrons or ions need to travel longer effective distances compared to diffusion in solid bulk medium. It is important to note that almost all transport of ions is present in the pore phase, however to give a comprehensive analysis of the virtual cathodes, τ_{fac} is determined for both phases $A \in \{\mathcal{A}, \mathcal{A}^{\mathsf{c}}\}$.

While the tortuosity factor quantifies the penalty induced by the heterogeneous microstructure on the effective diffusion, it does not provide insights on the geometric features responsible for its particular value. Tortuosity factor is an all-in-one parameter that encompasses the contributions of several features of the pore domain. In addition to the volume available for the diffusion itself (i.e., the porosity), two other metrics quantifying geometrically the sinuosity and the constriction of the diffusion paths have been introduced in the literature [21, 64] in an attempt to deconvolute their respective contributions to the effective diffusivity. Both are defined in the following.

Bruggeman exponent: An additional transport-related descriptor, directly derived from the tortuosity factor τ_{fac} and the volume fraction ε, is the so called Bruggeman exponent α, which is given by

$$\alpha(A) = \frac{\log\big(\varepsilon(A)/\tau_{\text{fac}}(A)\big)}{\log(\varepsilon(A))}.$$

Note that this descriptor can be directly obtained from the previously introduced descriptors, however it provides a more accessible interpretation. A value of $\alpha = 1.5$ corresponds to a medium composed of spherical, non-touching particles within A, whereas increasing values of α indicate less regular and more complex morphologies [65].

Geodesic tortuosity: The mean geodesic tortuosity τ_{geo} of a phase A quantifies the deviation of shortest paths within A from straight lines [53]. The tortuosity of a path is defined as the ratio of the actual path length to the straight-line distance between its endpoints. By definition, this ratio is always at least 1, with higher values indicating more tortuous paths. In this paper, the mean geodesic tortuosity τ_{geo} is computed as the average tortuosity of all shortest paths starting on a designated plane (e.g., the top or bottom) of the cathode and ending at the opposite side.

To take structural gradients into account, τ_{geo} is calculated separately for both directions (top-to-bottom and bottom-to-top). For a given direction, the shortest path from each integer-valued position of the phase on the starting plane to the target plane of the cathode is determined using Dijkstra's algorithm [66]. Starting positions that are not connected to the opposite side are excluded from the computation of τ_{geo}, i.e., τ_{geo} reflects only the tortuosity and not the number of paths. Each path length is then normalized by the straight-line distance between the two opposing planes. The mean geodesic tortuosity τ_{geo} is defined as the average of these normalized path lengths.

Analogous to the tortuosity factor τ_{fac}, the mean geodesic tortuosity τ_{geo} is determined for both phases $A \in \{\mathcal{A}, \mathcal{A}^{\mathsf{c}}\}$.

Maximum inscribed radius: To characterize the typical size of a phase, the maximum inscribed radius $r_{\max}$ is utilized. This descriptor represents the largest radius of spheres that can cover at least 50% of the volume fraction of the considered phase, with the spheres being fully contained within that phase. This metric is derived from the calculation of the so-called continuum particle- or phase-size distribution [67]. More precisely, for a phase $A \subset W$ let

$$O_r(A) = \{x \in A \colon B(x, r) \cap A^{\mathsf{c}} = \emptyset\},$$

denote the set of centers $x \in A$ where balls $B(x, r)$ of radius $r > 0$ can be placed while not intersecting the other phase A^{c}. The corresponding set, which is coverable with balls of radius r is obtained by dilating $O_r(A)$ with a ball of radius r, i.e.,

$$O_r(A) \oplus B(0, r) = \{x \in W \colon \text{ there is a } y \in O_r(A) \text{ with } x \in B(y, r)\},$$

where $\oplus$ denotes the dilation operator. Then the maximum inscribed radius $r_{\max}$ is given by

$$r_{\max}(A) = \sup\big\{r > 0 \colon \varepsilon\big(O_r(A) \oplus B(0, r)\big) \geq 0.5\big\}.$$

The maximum inscribed radius $r_{\max}$ and the subsequently introduced minimum intrusion radius $r_{\min}$ are numerically estimated utilizing the algorithm provided in [68].

Minimum intrusion radius: The minimum intrusion radius $r_{\min}$ quantifies the effect of narrow constrictions or bottlenecks in a phase along a given direction. It is defined as the largest radius of balls such that at least 50% of the phase volume can be covered by balls intruded from one side. More precisely, for an intrusion plane $\Pi = [0, 250] \times \{y\} \times [0, 250]$ (with $y = 0$ for the bottom or $y = 250$ for the top of the observation window W), consider

the set of centers connected to Π, i.e.,

$$Q_r(A,\Pi) = \{x \in O_r(A) \colon \text{there exists a path in } O_r(A) \text{ from } x \text{ to } \Pi\},$$

for an $r > 0$. The corresponding set of points coverable with the intrusion of balls with radius r from Π is derived by dilation of $Q_r(A,\Pi)$. Thus, $r_{\min}$ is given by

$$r_{\min}(A,\Pi) = \sup\{r > 0 \colon \varepsilon\big((Q_r(A,\Pi) \oplus B(0,r)) \cap W\big) \geq 0.5\}.$$

By construction, $r_{\min}(A,\Pi) \leq r_{\max}(A)$.

In applications due to computational efficiency, O_r and Q_r are evaluated only on an integer-valued grid.

Constrictivity: Constrictivity aims at quantifying the impact of section area variation along the diffusion paths on the effective diffusivity. Note that the constrictivity is a challenging metric to calculate, since the lack of a unique definition of large (bulge) and small (bottleneck) regions in a continuous domain. Because of this, several definitions have been provided in the literature [21, 64]. In this work, the constrictivity $\beta(A) = \frac{r_{\min}(A,\Pi)^2}{r_{\max}(A)^2} \in (0,1]$ of a phase $A \subset W$ and an intrusion plane $\Pi \subset W$ is defined as the squared ratio between the minimum intrusion radius $r_{\min}$ and the maximum inscribed radius $r_{\max}$, providing a normalized measure of how restrictive the narrowest bottlenecks are relative to the overall phase size [54]. A value of 1 corresponds to no bottleneck effects at all, while a value close to 0 corresponds to extreme bottleneck effects [58].

Chord length: Another insightful geometric characteristic for transport is the chord length distribution. A chord is a line segment lying entirely within a given phase A that cannot be extended in either direction without crossing into the complementary phase. The chord length distribution captures the spatial extent of the phase. In particular, longer chords correlate positively with favorable transport properties.

Since the present paper considers transport only in the vertical direction, only vertically aligned chords are investigated. In practice, due to computational efficiency, the chord length distribution is estimated through discretization. For this purpose, let $c = \{(x,y,z),(x,y+1,z),\dots,(x,y',z)\} \subset A$ with $x,y,y',z \in \{1,\dots,250\}$, $y \leq y'$, $(x,y-1,z),(x,y'+1,z) \notin A$, be a discretized chord. Then, its length ℓ is given by $\ell(c) = y' - y + 1$. The empirical probability distribution of these chord lengths then serves as an estimator for the chord length distribution. Considering the length-weighted distribution of these chords gives the chord length distribution; i.e., a chord of length $\ell(c)$ is counted $\ell(c)$ times, thereby accounting for the stronger influence of longer chords on geometry and transport. For a formal definition, refer to [40, 69].

3 Results and Discussion

In this section, the transport-related descriptors and effective properties defined in Section 2.4 are analyzed for differently structured cathodes. Due to the limited field of view of the experimentally imaged RP cathode, only one marked tessellation $\mathcal{T}$ of reasonable size could be fitted. The RP fragment phase and consequently $\mathcal{T}$, exhibit minor anisotropy with respect to the transport direction (y-direction), caused by manufacturing, particularly drying and calendaring. To avoid transferring this anisotropy onto the geometric and effective descriptors, we additionally consider virtual cathodes, based on $\mathcal{T}'$, which is derived by reflecting $\mathcal{T}$ at the x-z plane. Complementarily, ten pristine particle phases $\mathcal{P}^{(1)}, \ldots, \mathcal{P}^{(10)}$ were generated. For both structuring scenarios, "uniform" and "gradient", 20 realizations per recycling fraction $\eta \in \{0, 0,05, 0.1, 0.15, 0.2, 0.3, \ldots, 0.9, 1\}$ were obtained by combining the two RP fragment phases $\mathcal{T}, \mathcal{T}'$ with the ten pristine particle phases $\mathcal{P}^{(1)}, \ldots, \mathcal{P}^{(10)}$.

Note that low recycling fractions η are of particular relevance in view of the recycling quotas for Li-ion batteries planned by the European Union, which require at least 6 % recycled lithium, 6 % recycled nickel, and 16 % recycled cobalt in new batteries starting in 2031 [8]. Therefore, a finer subdivision of η in the low range is applied, while a larger step size is used for higher recycling fractions. However, the stochastic 3D microstructure model, described in Sections 2.1-2.3 is capable of generating virtual cathodes for any recycling fraction $\eta \in [0, 1]$.

In Figure 4, the deviation of the **volume fractions** of the pristine particle phase, RP fragment phase, and pore space is presented. The box plots indicate a low variance across the 20 realizations for each recycling fraction η. Further, the constant pore volume fraction implicitly confirms the constant total active material fraction. In addition, the volume fraction of pristine particles and RP fragments exhibits converse linear behavior, summing to $1 - \varepsilon(\mathcal{A}_\eta)$ for all η.

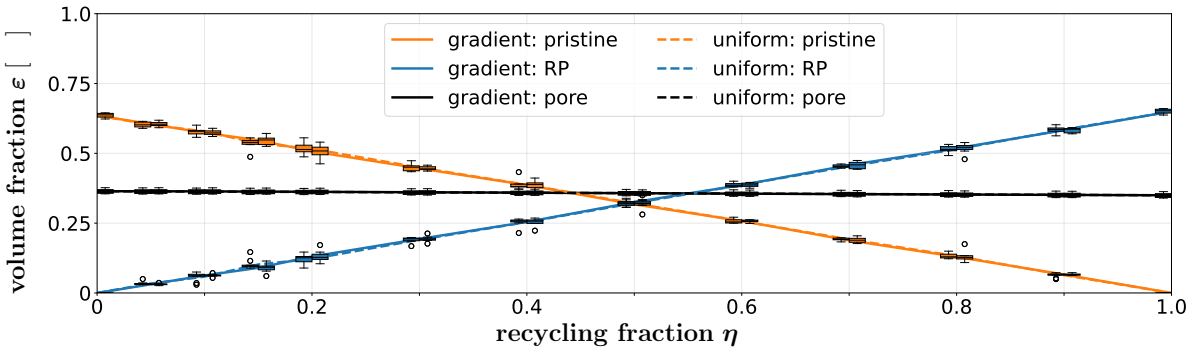

Figure 4: Box plots representing the distributions of the volume fractions of the pristine particle phase (orange), RP fragment phase (blue) and pore space (black). The "gradient" scenario is indicated utilizing solid lines and the "uniform" scenario with dashed lines (dashed and solid lines are nearly overlapping).

The box plots in Figure 5 show an increasing **specific surface area** for rising recycling fractions η for both structuring scenarios. This trend was expected, as the specific surface area is inversely correlated with the particle size [56]. Moreover, cathodes generated utilizing the "uniform" scenario consequently exhibit larger specific surface areas. This observation can be attributed to the fact that in the "gradient" scenario, the iterative replacement of pristine particles by RP fragments occurs predominantly layer by layer. As a result, many of the inserted RP fragments come into contact with others, which reduces the overall specific surface area. In contrast, the "uniform" scenario introduces RP fragments more evenly throughout the entire observation window W, leading to a more homogeneous distribution and fewer inter-particle contacts, thereby increasing the (specific) surface area.

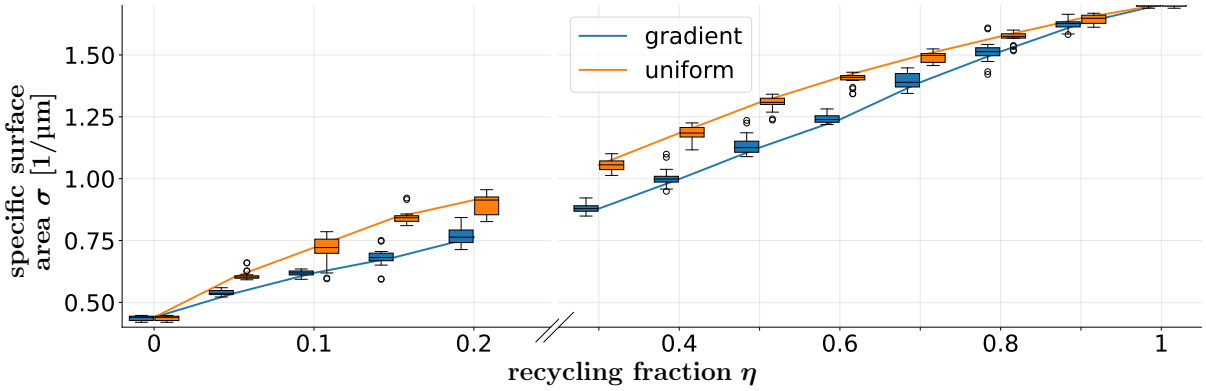

Figure 5: Box plots indicating the distribution of specific surface area for cathodes generated using both structuring scenarios, namely "gradient" (blue) and "uniform" (orange). Note that the breakage of the x-axis at $\eta = 0.25$ indicates differently scales of the intervals [0,0.25) and (0.25,1].

Figure 6 shows the **tortuosity factor** as a function of the recycling fraction η. For transport within the active material phase (Figure 6(a)), the tortuosity factor decreases monotonically with increasing η, indicating reduced diffusivity. Note that values corresponding to the "uniform" scenario are generally smaller than those of the "gradient" scenario.

In contrast, for transport within the pore space (Figure 6(b)), the tortuosity factor increases with increasing η, where values corresponding to the "uniform" scenario are larger than those of the "gradient" scenario.

It is important to note that the tortuosity factor of the active material phase decreases rapidly for $\eta \in [0, 0.2]$, compared to $\eta \in [0.2, 1]$. This implies that a low recycling fraction within the cathode can significantly increase the effective transport properties.

Complementarily, for low η the tortuosity factor in pore space increases only slightly, indicating a moderate deterioration of tortuosity factor properties. The tortuosity factor in the pore space increases with the recycling fraction (Figure 6(b)) at constant porosity

(Figure 4), which indicates a shift in the pore topology domain. That is, a transition from roughly spherical particles to a less ideal morphology is expected since the RP fragments are not spherical but polyhedral due to the underlying Voronoi tessellation. This shape transition is also confirmed by the Bruggeman exponent of the pore space, which is ≈ 1.5 for $\eta = 0$, and increases for increasing recycling fractions, see Figure 7.

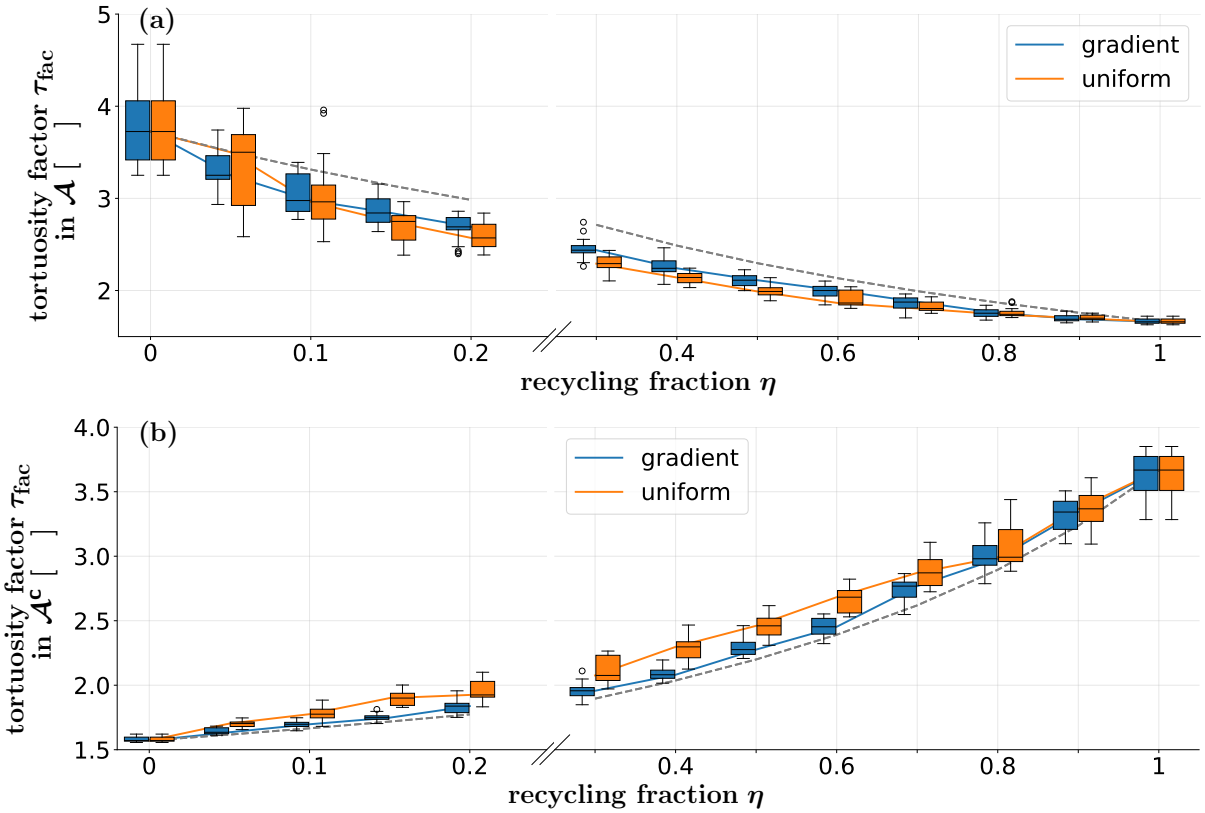

Figure 6: Box plots showing the change of the tortuosity factor for increasing recycling fraction η, where (a) indicates transport within the active material phase and (b) within the pore space. Results derived from the "gradient" scenario are indicated blue, whereas orange boxes represent the "uniform" scenario. The dashed lines indicate the theoretical values for a cathodes consisting of two well-separated layers.

The very high tortuosity factors calculated for large values of η, are slightly above the values calculated or measured for real NMC cathodes [21, 70]. This indicates that the voxel-based and tessellation-based representations of the RP phase somewhat underestimate the diffusivity in the pore space compared to experiments.

Additionally, in Figure 6, the tortuosity factor of a cathode, consisting of two well-separated layers with a recycling fraction $\eta \in [0, 1]$ is indicated by a dashed line. Formally, it is given by

$$\tau_{\text{fac}}^{\text{layered}}(\eta, A_0, A_1) = \frac{1}{\frac{\eta}{\tau_{\text{fac}}(A_1)} + \frac{1-\eta}{\tau_{\text{fac}}(A_0)}},$$

where $\tau_{\text{fac}}(A_0), \tau_{\text{fac}}(A_1)$ denotes the tortuosity factor of a cathode made solely out of

pristine particles and RP, respectively [71]. This theoretical line shows higher tortuosity factor values than those for both scenarios in the active material phase $\mathcal{A}$. For transport in pore space $\mathcal{A}^c$ the tortuosity factor τ_{fac} is slightly larger than the theoretical value of the layered cathode. This indicates that the influence of the interface between the two layers is not negligible.

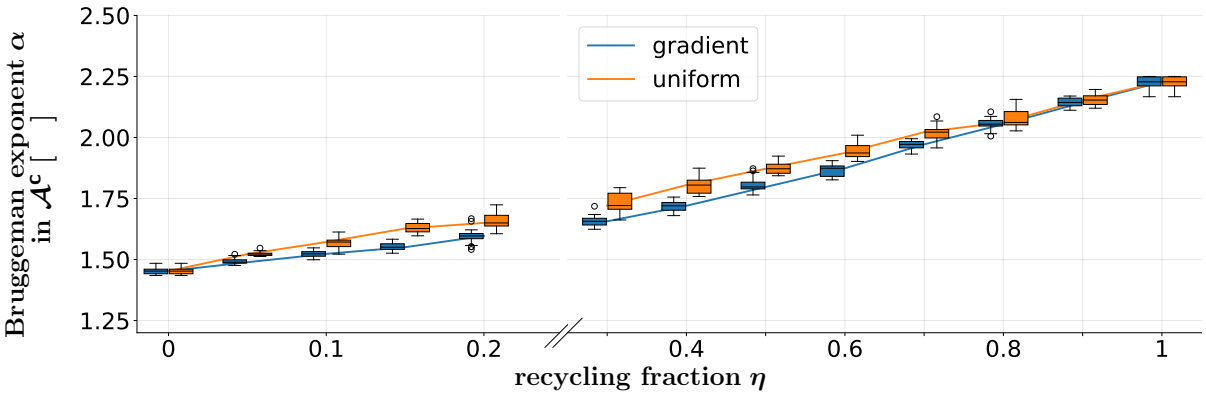

Figure 7: Boxplots indicating the distribution of the Bruggeman exponent for increasing recycling fractions η within the pore space. Results derived from the "gradient" scenario are indicated blue, whereas orange boxes represent the "uniform" scenario.

The **mean geodesic tortuosity** was determined within the active material phase in both the top-to-bottom direction and the bottom-to-top direction, see Figure 8(a). For both structuring scenarios, "uniform" and "gradient", the mean geodesic tortuosity decreases with increasing recycling fraction η. Indeed, as the particles get smaller, moving from one side to the other within the solid domain requires less direction changes as particles are closer to each other. However, tortuosity values corresponding to the "uniform" scenario are consistently smaller than those of the "gradient" scenario. While the "uniform" scenario exhibits directional symmetry, the "gradient" scenario reveals larger values for the top-to-bottom direction, corresponding to transport originating in the RP fragment-rich layer.

This asymmetry can be explained by the large difference in size between the pristine particles and RP fragments. There are fewer transport paths starting at the pristine-rich layer (bottom) to the RP fragment-rich layer (top) than vise versa. This effect is illustrated in Figure 9.

Additionally, pores tend to be larger between large pristine particles than between small RP fragments, as confirmed by the chord length distribution in the pore space, as shown in Figure 13(b). This implies that at the transition region between the layers, each pristine particle is more likely to be connected to a RP fragment than vice versa. Consequently, transport paths from the RP fragment layer to the pristine particle layer exhibit larger deviations than those in the opposite direction.

Additionally, the mean geodesic tortuosity was determined within the pore space in

the top-to-bottom direction as well as the bottom-to-top direction (Figure 8(b)). Here, an increasing recycling fraction η results in longer paths for both structuring strategies, since the initially unobstructed pore space becomes increasingly filled with obstacles (RP fragments). Again, in the "uniform" scenario there is a high similarity between both directions. However, these tortuosities are clearly smaller than the ones corresponding to the "gradient" scenario. Particularly, tortuosities corresponding to the "gradient" scenario in the bottom-to-top direction exhibit the highest values. Note that the mean geodesic tortuosity accounts only for the shortest paths from the starting plane to the target plane. It provides no information about the number of such paths. The low geodesic tortuosity values are in agreement with those determined geometrically in previous work for real electrodes [21].

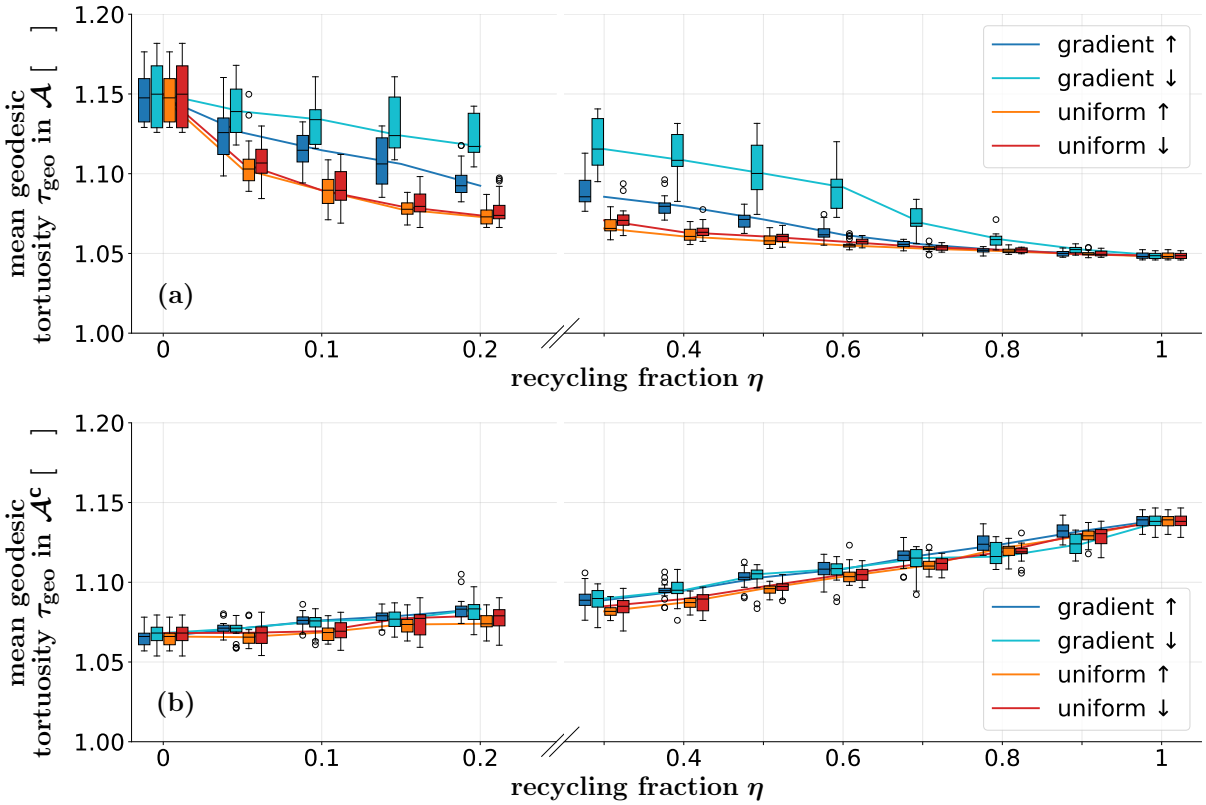

Figure 8: Box plots showing the distribution of mean geodesic tortuosity for various recycling fractions η in the active material phase (a) and pore space (b). Blue and cyan boxes correspond to the "gradient" scenario, while red and orange boxes represent the "uniform" scenario. The arrows indicate the direction of transport: upward-pointing arrows correspond bottom-to-top direction, and downward-pointing arrows to top-to-bottom direction.

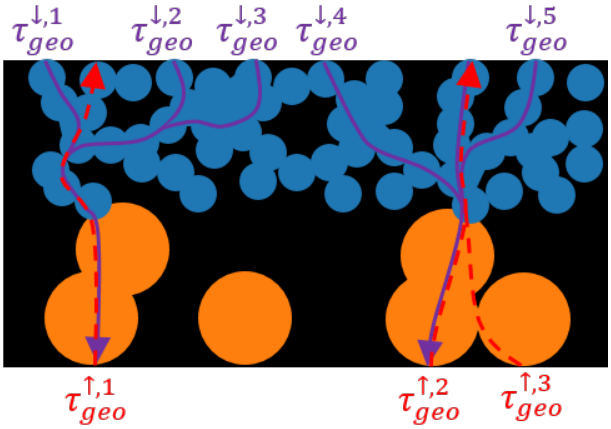

Figure 9: Sketch of 2D geodesic tortuosity asymmetry illustrated for the active material phase of the "gradient" scenario. Purple solid lines represent a selection of the shortest paths from top to bottom. Red dashed lines represent all shortest paths from bottom to top.

The **maximum inscribed radius** $r_{\max}$, determined in the active material phase, decreases with increasing recycling fraction η, as shown in Figure 10(a). A rapid drop is observable between $\eta = 0.4$ and $\eta = 0.5$. Since $r_{\max}$ describes the maximum radius of spheres that can cover at least 50% of the active material phase, the decline is expected. At $\eta = 0.5$ half of the active materials consists of RP fragments, which can only be covered by significantly smaller spheres. Similarly, $r_{\max}$ determined within the pore space also decreases for increasing recycling fractions of both structuring scenarios, see Figure 10 (b). However, the decrease is more pronounced for the "uniform" scenario. In this case, RP fragments are more likely to be inserted into large pores, whereas in the "gradient" scenario, RP fragments are introduced progressively from top to bottom, resulting in less disruption to large pores at lower layers.

The influence of different recycling fractions η on the **minimum intrusion radius** $r_{\min}$ is presented in Figure 11. As expected, values of $r_{\min}$ corresponding to the "uniform" scenario, determined in both transport directions, show a similar decrease for both phases, active material (Figure 11(a)) and pore space (Figure 11(b)). In contrast, for the "gradient" scenario, the top-to-bottom direction exhibits for both phases consequently smaller values compared to the bottom-to-top direction. This effect can be attributed to the layered structure of the "gradient" cathode, where for low recycling fractions only the top layers of the cathode are altered, e.g., pristine particles are removed and RP fragments are introduced. In particular, neither active material nor pore space at the bottom of the cathode is modified. Consequently, the intrusion of spheres into both the active material and pore space from the bottom is less affected compared to the "uniform" scenario, in which modifications occur throughout the entire volume.

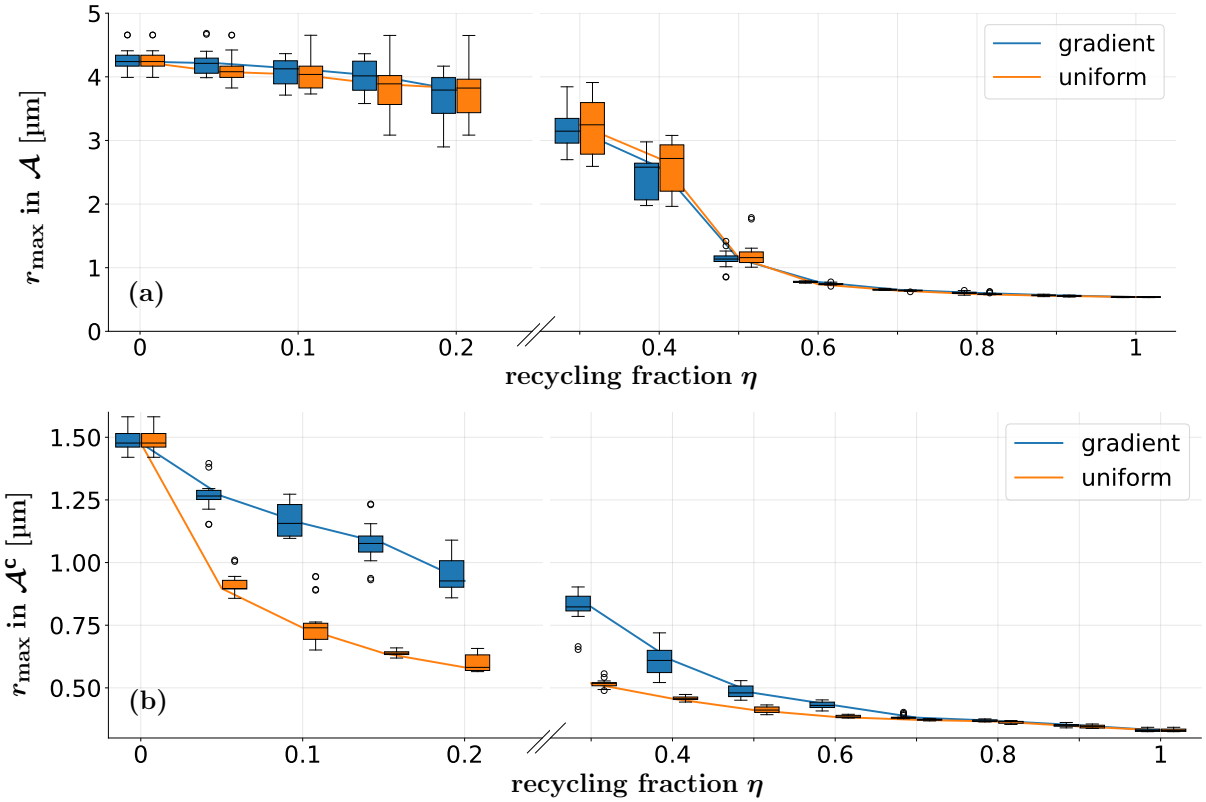

Figure 10: Box plots indicating the distribution of $r_{\max}$ depending on the recycling fraction η within the active material phase (a) and pore space (b). Blue boxes indicate the "gradient" scenario, whereas orange ones corresponds to the "uniform" scenario.

The **constrictivity** determined in the active material phase shows a similar behavior for cathodes generated using both the "uniform" and "gradient" scenarios, as well as for both transport directions, see Figure 12(a). For recycling fractions $\eta \in [0, 0.4]$, the constrictivity remains around 0.05, indicating very strong bottleneck effects. This can be attributed to the fact that in this range more than 50% of the active material volume is present in pristine NMC particles.

Although these particles exhibit a large diameter, their near-spherical shape leads to only comparatively small contact areas with each other, which results in pronounced bottleneck effects. When the fraction of added RP fragment exceeds 50%, meaning that more than half of the active material phase is present in the fine-granular structure of the RP fragment phase, the bottleneck effects are reduced. This reduction arises from the absence of regions in the RP fragment phase in which balls with a large radius $r_{\max}$ fit.

In contrast, the constrictivity determined within the pore space shows pronounced differences between the "uniform" and "gradient" scenarios, see Figure 12(b). For the "uniform" cathodes, no clear directional trends are visible. In both directions, a monotonous decrease in bottleneck effects can be observed, which is associated with the reduction of extremely large pores. In the "gradient" cathode, however, much stronger bottleneck effects occur from top to bottom compared to the "uniform" case, as long as the fraction

of recycled material remains below 50%. This effect can be explained by the presence of large pores, that account for more than 50% of the total pore volume, in the lower half of the cathode. These pores are separated from the top of the cathode by a fine porous RP fragment layer, which forms the bottleneck towards large pores. For bottleneck effects in the opposite direction, i.e., from bottom to top, the situation differs: here, no fine porous barrier has to be traversed, and thus, no significant bottleneck effects arise. Moreover, since no scattered small RP fragments are present in the large pores between pristine particles, the bottleneck effects are even weaker than in the "uniform" scenario. This holds true even for small fractions of recycled material.

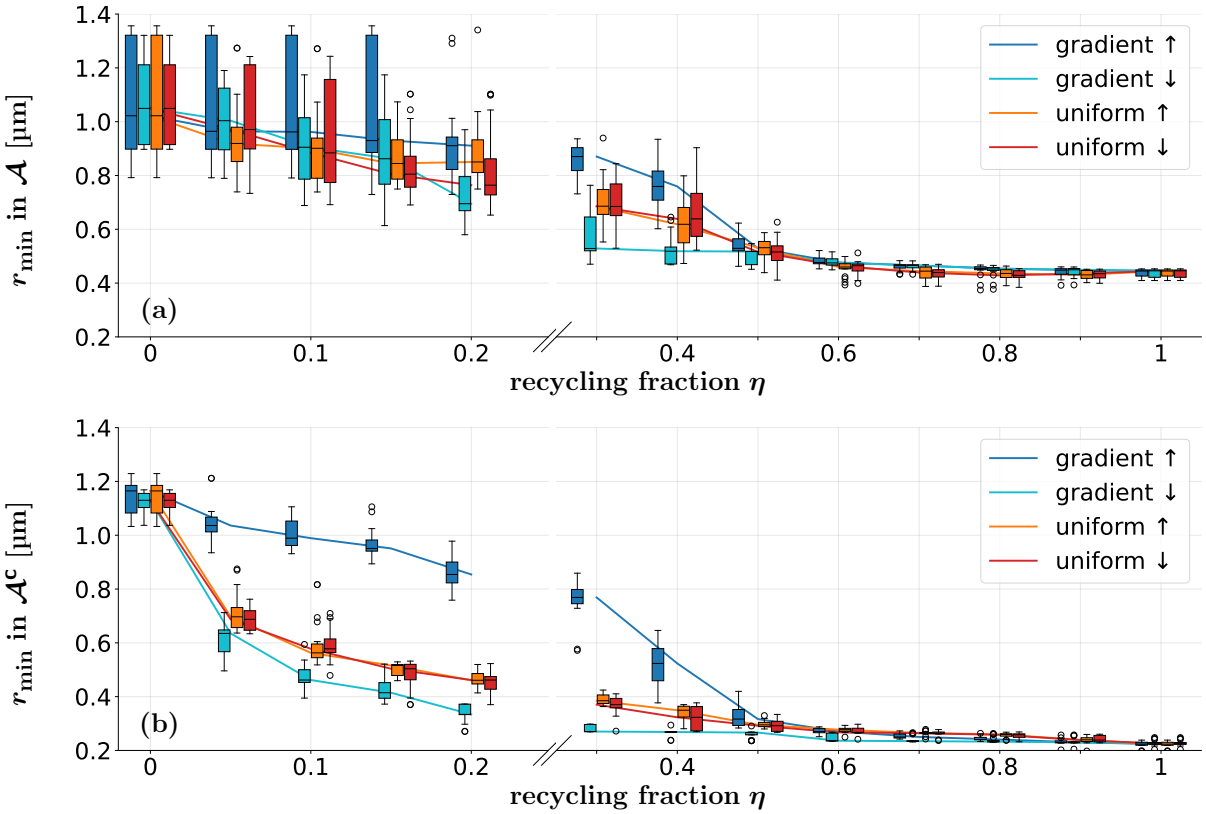

Figure 11: Box plots showing the distribution of $r_{\min}$ within active material (a) and pore space (b). Blue and cyan boxes represent the "gradient" scenario, while red and orange boxes correspond to the "uniform" scenario.

The **chord length** distribution was determined for both the active material (Figure 13(a)) and the pore space (Figure 13(b)). In both phases, the chord length distribution shows similar behavior for the "uniform" and the "gradient" scenarios, whereas chords in the pore space are on average slightly smaller for the uniform scenario than for the gradient scenario.

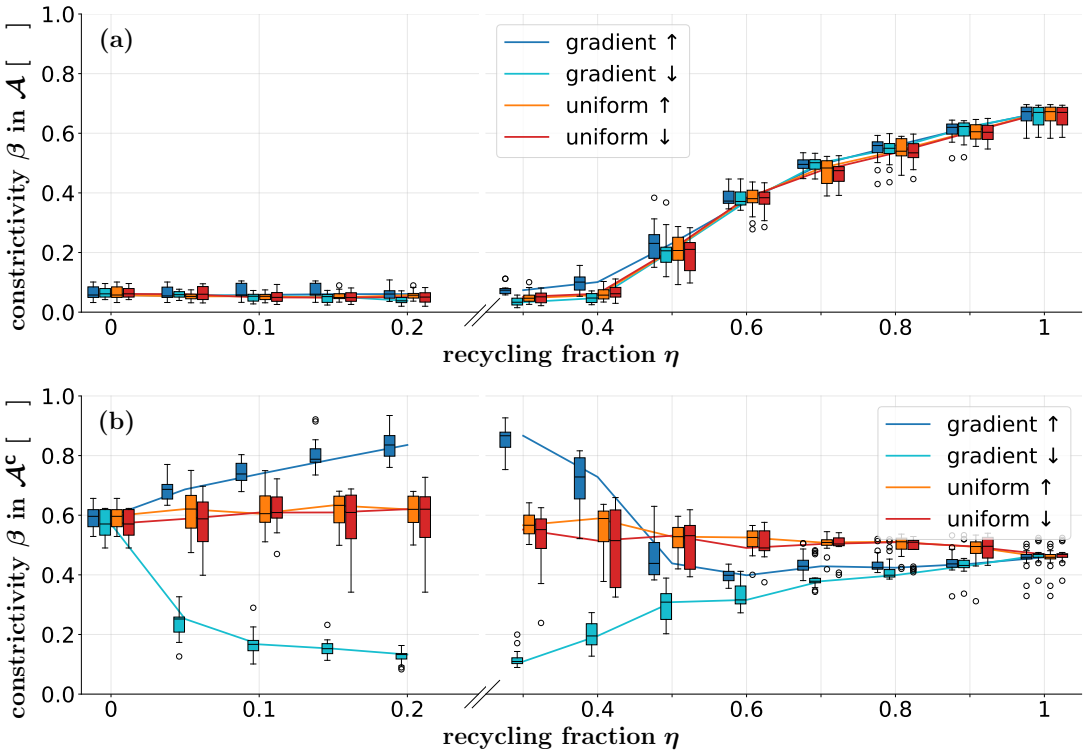

Figure 12: Box plots indication the distribution of constrictivity values for the "gradient" (blue and cyan) and "uniform" (red and orange) scenario for increasing recycling fractions m. Constrictivity values determined in the active material phase are presented in (a), while (b) considers the pore space.

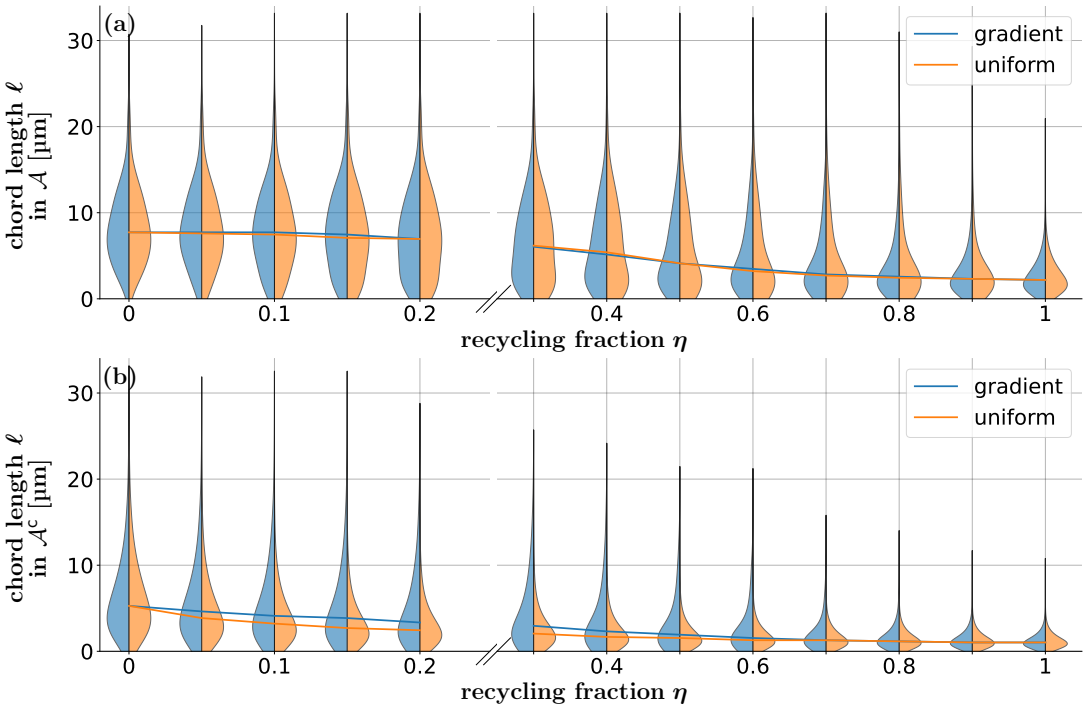

Figure 13: Violin plots visualizing the chord length distribution for both structuring scenarios, namely "gradient" (blue) and "uniform" (orange), in the active material (a) and the pore space (b). The blue and orange lines show the corresponding median values.

4 Conclusion

This work presented a novel computational framework for systematically investigating structure-property relationships of lithium-ion battery cathodes containing mixtures of pristine and recycled NMC particles. Recycled particle fragments are generally smaller than pristine particles, as they arise from recycling processes that break EOL particles into clusters of, or even individual, primary particles. A stochastic 3D microstructure model combines spherical harmonic-based representations for pristine particles with marked Voronoi tessellation-based representations for recycled particle fragments, enabling the generation of cathodes with arbitrary mixing ratios of both active material types. Additionally, the model allows for different structural configurations, as demonstrated by two types of mixing considered in this paper, namely, uniform and gradient mixtures of particles. The proposed microstructure model is embedded within a virtual material testing framework that quantifies the morphology and effective transport-related properties of generated microstructures, assuming that pristine particles and recycled particle fragments do not differ in their chemical or electrochemical properties.

This statistical analysis revealed several key insights into how the incorporation of recycled active material affects cathode microstructure and transport properties. The results demonstrate that even low recycling fractions (below 20%) induce substantial changes in transport-related descriptors within the pore space, while the transport properties of the active material phase remain relatively stable in this range. In particular, the specific surface area increased monotonically with increasing recycling fraction for both structuring scenarios, with the "uniform" scenario consistently yielding larger values due to reduced inter-particle contact between recycled particle fragments. This increased interfacial area potentially enhance charge transfer kinetics, as a greater reactive surface is available for electrochemical reactions.

The analysis of the tortuosity factor revealed contrasting trends between the two phases. In the active material phase, the tortuosity factor decreased substantially with increasing fraction of recycled particles, especially for small recycling fractions, indicating improved electronic transport pathways as pristine particles were replaced by the finer-grained RP fragment network. Conversely, the tortuosity factor in the pore space increased with increasing recycling fraction, reflecting a shift from nearly ideal spherical particle morphology (Bruggeman exponent ≈ 1.5 for pure pristine cathodes) toward more complex, broken particle geometries. Notably, the "uniform" scenario exhibits lower tortuosities in the active material phase and higher tortuosities in the pore space compared to the "gradient" scenario, highlighting the importance of the spatial arrangement of the RP fragments.

The analysis of the mean geodesic tortuosity revealed that transport paths in the active material phase become shorter and less tortuous with increasing recycling fraction, as

smaller RP fragments promote more direct particle connectivity. However, the "gradient" scenario exhibits pronounced directional asymmetry, with paths originating from the RP fragment-rich layer showing higher tortuosity values. This asymmetry, caused by the size mismatch between pristine particles and RP fragments, suggests that orientation of such layers could be optimized to favor specific transport directions in electrode designs.

From a sustainability perspective, especially in view of European Union recycling quotas requiring batteries to contain at least 6% recycled lithium, 6% recycled nickel, and 16% recycled cobalt by 2031, the presented findings have important implications. Our results indicate that even low fractions of recycled NMC can substantially affect transport properties within the pore space while potentially enhancing connectivity within the active material. Furthermore, different structuring strategies offer optimization opportunities: the "uniform" scenario provides relatively homogeneous properties and a larger reactive surface area, while the "gradient" approach enables targeted directional transport optimization.

The carbon-binder domain was intentionally excluded from the presented model to reduce variability and isolate the effects arising solely from differences in the composition and arrangement of the active material phase. Future work should investigate the spatial distribution of the carbon-binder domain within mixed cathodes and evaluate its influence on electronic conductivity and mechanical integrity. Additionally, while this study focused on geometric and effective transport descriptors, electrochemical performance metrics such as rate capability and cycling stability remain to be investigated through coupled electrochemical-microstructural simulations. The presented computational framework could directly be extended to other cathode chemistries, enabling broader applicability. Summing up, the observed sensitivity of transport properties to both recycling fraction and structuring strategy emphasizes the importance of careful microstructure design in sustainable battery manufacturing.

Author contributions

Lukas Fuchs Writing – original draft, Visualization, Software, Methodology, Investigation, Formal analysis, Conceptualization. **Philipp Rieder** Writing – original draft, Visualization, Software, Methodology, Investigation, Formal analysis, Conceptualization. **Donal P. Finegan** Writing – review & editing, Supervision, Conceptualization, Data curation. **Francois Usseglio-Viretta** Writing – review & editing, Visualization, Methodology. **Jeffrey Allen** Writing – review & editing, Methodology. **Melissa Popeil** Data curation, Writing – review & editing. **Orkun Furat** Writing – review & editing, Supervision, Conceptualization. **Volker Schmidt** Writing – review & editing, Supervision, Resources, Project administration, Conceptualization.

Acknowledgments

This work was authored in part by the Alliance for Energy Innovation, LLC, the manager and operator of the National Laboratory of the Rockies for the U.S. Department of Energy (DOE) under Contract No. DE-AC36-08GO28308. Funding was provided by the DOE's Vehicle Technologies Office, Extreme Fast Charge, and Cell Evaluation of Lithium-ion Batteries Program, Jake Herb, Technology Manager. The views expressed in the article do not necessarily represent the views of the DOE or the U.S. Government. The U.S. Government retains and the publisher, by accepting the article for publication, acknowledges that the U.S. Government retains a nonexclusive, paid-up, irrevocable, worldwide license to publish or reproduce the published form of this work, or allow others to do so, for U.S. Government purposes.

Data Availability Statement

The datasets generated during and/or analyzed during the current study are available from the corresponding authors on reasonable request.

References

[1] International Energy Agency. Global EV outlook 2025: Electric vehicle batteries. Technical report, International Energy Agency, 2025. URL `https://www.iea.org/reports/global-ev-outlook-2025/electric-vehicle-batteries`. Accessed: 2025-10-16.

[2] International Energy Agency. Global EV outlook 2023: Trends in batteries. Technical report, International Energy Agency, 2023. URL `https://www.iea.org/reports/global-ev-outlook-2023/trends-in-batteries`. Accessed: 2025-10-16.

[3] X. Lu, A. Bertei, D. P. Finegan, C. Tan, S. R. Daemi, J. S. Weaving, K. B. O'Regan, T. M. Heenan, G. Hinds, E. Kendrick, D. J. L. Brett, and P. R. Shearing. 3D microstructure design of lithium-ion battery electrodes assisted by X-ray nano-computed tomography and modelling. *Nature Communications*, 11:2079, 2020.

[4] E. A. Olivetti, G. Ceder, G. G. Gaustad, and X. Fu. Lithium-ion battery supply chain considerations: Analysis of potential bottlenecks in critical metals. *Joule*, 1: 229–243, 2017.

[5] International Energy Agency. Growing geopolitical tensions underscore the need for stronger action on critical minerals security, 2025. URL

https://www.iea.org/commentaries/growing-geopolitical-tensions-underscore-the-need-for-stronger-action-on-critical-minerals-security. Accessed: 2025-10-16.

[6] Y. Miao, L. Liu, Y. Zhang, Q. Tan, and J. Li. An overview of global power lithium-ion batteries and associated critical metal recycling. *Journal of Hazardous Materials*, 425:127900, 2022.

[7] J. Lin, E. Fan, X. Zhang, R. Chen, F. Wu, and L. Li. Sustainable recycling of cathode scrap towards high-performance anode materials for Li-ion batteries. *Advanced Energy Materials*, 12:2103288, 2022.

[8] European Union. Regulation (EU) 2023/1542 of the European Parliament and of the Council of 12 July 2023 concerning batteries and waste batteries, amending Directive 2008/98/EC and Regulation (EU) 2019/1020 and repealing Directive 2006/66/EC. https://eur-lex.europa.eu/legal-content/EN/TXT/?uri=CELEX:32023R1542, 2023.

[9] J. Xiao, J. Li, and Z. Xu. Challenges to future development of spent lithium ion batteries recovery from environmental and technological perspectives. *Environmental Science & Technology*, 54:9–25, 2019.

[10] M. Chen, X. Ma, B. Chen, R. Arsenault, P. Karlson, N. Simon, and Y. Wang. Recycling end-of-life electric vehicle lithium-ion batteries. *Joule*, 3:2622–2646, 2019.

[11] B. Makuza, Q. Tian, X. Guo, K. Chattopadhyay, and D. Yu. Pyrometallurgical options for recycling spent lithium-ion batteries: A comprehensive review. *Journal of Power Sources*, 491:229622, 2021.

[12] J.-P. Harvey, W. Courchesne, M. D. Vo, K. Oishi, C. Robelin, U. Mahue, P. Leclerc, and A. Alhaiek. Greener reactants, renewable energies and environmental impact mitigation strategies in pyrometallurgical processes: A review. *MRS Energy & Sustainability*, 9:212–247, 2022.

[13] Y. Yao, M. Zhu, Z. Zhao, B. Tong, Y. Fan, and Z. Hua. Hydrometallurgical processes for recycling spent lithium-ion batteries: A critical review. *ACS Sustainable Chemistry & Engineering*, 6:13611–13627, 2018.

[14] N. Hayagan, C. Aymonier, L. Croguennec, M. Morcrette, R. Dedryvère, J. Olchowka, and G. Philippot. A holistic review on the direct recycling of lithium-ion batteries from electrolytes to electrodes. *Journal of Materials Chemistry A*, 12:31685–31716, 2024.

[15] P. Tembo, C. Dyer, and V. Subramanian. Lithium-ion battery recycling—a review of the material supply and policy infrastructure. *NPG Asia Materials*, 16:43, 2024.

[16] M. Popeil, F. Usseglio-Viretta, X. Pu, P. Gasper, N. Dutta, E. Wang, E. Allen, J. Mangum, N. Sunderlin, K. Fink, J. Allen, P. Weddle, S. DeCaluwe, and D. Finegan. Heterogeneity of the dominant causes of performance loss in end-of-life cathodes and their consequences for direct recycling. *Advanced Energy Materials*, 15:2405371, 2025.

[17] D. P. Finegan, A. Vamvakeros, C. Tan, T. M. M. Heenan, S. R. Daemi, N. Seitzman, M. Di Michiel, S. Jacques, A. M. Beale, D. J. L. Brett, P. R. Shearing, and K. Smith. Spatial quantification of dynamic inter and intra particle crystallographic heterogeneities within lithium ion electrodes. *Nature Communications*, 11:631, 2020.

[18] M. Ebner, F. Marone, M. Stampanoni, and V. Wood. Visualization and quantification of electrochemical and mechanical degradation in Li ion batteries. *Science*, 342:716–720, 2013.

[19] B. Prifling, L. Fuchs, A. Yessim, M. Osenberg, M. Paulisch-Rinke, P. Zimmer, M. D. Hager, U. S. Schubert, I. Manke, T. Carraro, and V. Schmidt. Correlating the 3D morphology of polymer-based battery electrodes with effective transport properties. *ACS Applied Materials & Interfaces*, 16:66571–66583, 2024.

[20] M. Neumann, M. Ademmer, M. Osenberg, A. Hilger, F. Wilde, S. Muench, M. D. Hager, U. S. Schubert, I. Manke, and V. Schmidt. 3D microstructure characterization of polymer battery electrodes by statistical image analysis based on synchrotron X-ray tomography. *Journal of Power Sources*, 542:231783, 2022.

[21] F. L. Usseglio-Viretta, D. P. Finegan, A. Colclasure, T. M. Heenan, D. Abraham, P. Shearing, and K. Smith. Quantitative relationships between pore tortuosity, pore topology, and solid particle morphology using a novel discrete particle size algorithm. *Journal of The Electrochemical Society*, 167:100513, 2020.

[22] J. Song, R. C. Ihuaenyi, J. Lim, Z. Wang, W. Li, R. Fang, A. K. Ghamsari, H. Xu, Y. M. Lee, and J. Zhu. A microstructural electrochemo-mechanical model of high-nickel composite electrodes towards digital twins to bridge the particle and electrode-level characterizations. *Energy & Environmental Science*, 18:3129–3147, 2025.

[23] S. J. Cooper, A. Bertei, P. R. Shearing, J. Kilner, and N. P. Brandon. Taufactor: An open-source application for calculating tortuosity factors from tomographic data. *SoftwareX*, 5:203–210, 2016.

[24] A. G. Kashkooli, A. Amirfazli, S. Farhad, D. U. Lee, S. Felicelli, H. W. Park, K. Feng, V. De Andrade, and Z. Chen. Representative volume element model of lithium-ion

battery electrodes based on X-ray nano-tomography. *Journal of Applied Electrochemistry*, 47:281–293, 2017.

[25] T.-T. Nguyen, A. Demortière, B. Fleutot, B. Delobel, C. Delacourt, and S. J. Cooper. The electrode tortuosity factor: why the conventional tortuosity factor is not well suited for quantifying transport in porous Li-ion battery electrodes and what to use instead. *npj Computational Materials*, 6:123, 2020.

[26] M. E. Ferraro, B. L. Trembacki, V. E. Brunini, D. R. Noble, and S. A. Roberts. Electrode mesoscale as a collection of particles: Coupled electrochemical and mechanical analysis of NMC cathodes. *Journal of The Electrochemical Society*, 167:013543, 2020.

[27] Y. Takagishi, T. Yamanaka, and T. Yamaue. Quasi-3D modeling of Li-ion batteries based on single 2D image. *SN Applied Sciences*, 3:633, 2021.

[28] S. Cooper, D. Eastwood, J. Gelb, G. Damblanc, D. Brett, R. Bradley, P. Withers, P. Lee, A. Marquis, N. Brandon, and P. Shearing. Image based modelling of microstructural heterogeneity in $LiFePO_4$ electrodes for Li-ion batteries. *Journal of Power Sources*, 247:1033–1039, 2014.

[29] J. Joos, A. Buchele, A. Schmidt, A. Weber, and E. Ivers-Tiffée. Virtual electrode design for lithium-ion battery cathodes. *Energy Technology*, 9:2000891, 2021.

[30] L. Fuchs, O. Furat, D. P. Finegan, J. Allen, F. L. Usseglio-Viretta, B. Ozdogru, P. J. Weddle, K. Smith, and V. Schmidt. Generating multi-scale Li-ion battery cathode particles with radial grain architectures using stereological generative adversarial networks. *Communications Materials*, 6:4, 2025.

[31] P. Rieder, O. Furat, F. L. Usseglio-Viretta, J. Allen, P. J. Weddle, D. P. Finegan, K. Smith, and V. Schmidt. Stochastic 3D reconstruction of cracked polycrystalline NMC particles using 2D SEM data. *npj Computational Materials*, 11:232, 2025.

[32] F. Cadiou, T.-T. Nguyen, M. Bettge, Z. Su, J. Ando, V. De Andrade, D. Miller, and A. Demortière. Morphological evolution of NMC secondary particles through in situ electrochemical FIB/SEM experiment. *Preprint available at arXiv:2208.00878*, 2022.

[33] R. Martineau. A deeper look at hidden damage: Nano-CT imaging maps internal battery degradation. *Advanced Manufacturing Research — NREL*, June 2025. URL `https://www.nrel.gov/manufacturing/news/program/2025/a-deeper-look-at-hidden-damage--nano-ct-imaging-maps-internal-battery-degradation`. Last updated: January 9, 2025.

[34] C. Cheng, R. Drummond, S. R. Duncan, and P. S. Grant. Micro-scale graded electrodes for improved dynamic and cycling performance of Li-ion batteries. *Journal of Power Sources*, 413:59–67, 2019.

[35] P. Gräfensteiner, E. Löwer, O. Furat, U. A. Peuker, and V. Schmidt. Artificial filter cake generation: Digital twins via stochastic 3D modeling based on µ-CT image data. *Powder Technology*, 452:120550, 2025.

[36] J. Mościński, M. Bargieł, Z. A. Rycerz, and P. W. M. Jacobs. The force-biased algorithm for the irregular close packing of equal hard spheres. *Molecular Simulation*, 3:201–212, 1989.

[37] A. Bezrukov, M. Bargieł, and D. Stoyan. Statistical analysis of simulated random packings of spheres. *Particle & Particle Systems Characterization*, 19:111–118, 2002.

[38] S. Asmussen and P. W. Glynn. *Stochastic Simulation: Algorithms and Analysis*. Springer, 2007.

[39] Y. Bai, L. Yu, and I. Belharouak. Sequential separation of battery electrode materials and metal foils in aqueous media. *Journal of Power Sources*, 592:233954, 2024.

[40] S. Chiu, D. Stoyan, W. S. Kendall, and J. Mecke. *Stochastic Geometry and its Applications*. J. Wiley & Sons, 3rd edition, 2013.

[41] Z. Pawlas, I. Karafiátová, and L. Heller. Random tessellations marked with crystallographic orientations. *Spatial Statistics*, 39:100469, 2020.

[42] O. Furat, L. Petrich, D. P. Finegan, D. Diercks, F. Usseglio-Viretta, K. Smith, and V. Schmidt. Artificial generation of representative single Li-ion electrode particle architectures from microscopy data. *npj Computational Materials*, 7:105, 2021.

[43] P. Rieder, M. Neumann, L. Monteiro Fernandes, A. Mulard, H. Proudhon, F. Willot, and V. Schmidt. Stochastic 3D microstructure modeling of twinned polycrystals for investigating the mechanical behavior of γ-TiAl intermetallics. *Computational Materials Science*, 238:112922, 2024.

[44] L. Petrich, O. Furat, M. Wang, C. E. Krill III, and V. Schmidt. Efficient fitting of 3D tessellations to curved polycrystalline grain boundaries. *Frontiers in Materials*, 8:760602, 2021.

[45] S. Bock, J. Goppold, and M. Weiß. An improvement of the convergence proof of the ADAM-Optimizer. *Preprint available at arXiv:1804.10587*, 2018.

[46] T. Kanungo, D. M. Mount, N. S. Netanyahu, C. D. Piatko, R. Silverman, and A. Y. Wu. An efficient k-means clustering algorithm: Analysis and implementation. *IEEE Transactions on Pattern Analysis and Machine Intelligence*, 24:881–892, 2002.

[47] M. Fiedler and A. Alpers. Power-SLIC: Fast superpixel segmentations by diagrams. *Preprint available at arXiv:2012.11772*, 2020.

[48] M. Cheriet, J. N. Said, and C. Y. Suen. A recursive thresholding technique for image segmentation. *IEEE Transactions on Image Processing*, 7:918–921, 1998.

[49] M. Mafi, H. Martin, M. Cabrerizo, J. Andrian, A. Barreto, and M. Adjouadi. A comprehensive survey on impulse and gaussian denoising filters for digital images. *Signal Processing*, 157:236–260, 2019.

[50] R. Docherty, I. Squires, A. Vamvakeros, and S. J. Cooper. SAMBA: A trainable segmentation web-app with smart labelling. *Journal of Open Source Software*, 9: 6159, 2024.

[51] S. Berg, D. Kutra, T. Kroeger, C. N. Straehle, B. X. Kausler, C. Haubold, M. Schiegg, J. Ales, T. Beier, M. Rudy, et al. Ilastik: interactive machine learning for (bio) image analysis. *Nature Methods*, 16:1226–1232, 2019.

[52] T. Dabat, A. Mazurier, F. Hubert, E. Tertre, B. Grégoire, B. Dazas, and E. Ferrage. Mesoscale anisotropy in porous media made of clay minerals. A numerical study constrained by experimental data. *Materials*, 11:1972, 2018.

[53] L. Holzer, P. Marmet, M. Fingerle, A. Wiegmann, M. Neumann, and V. Schmidt. *Tortuosity and Microstructure Effects in Porous Media: Classical Theories, Empirical Data and Modern Methods*. Springer Nature, 2023.

[54] D. Wiedenmann, L. Keller, L. Holzer, J. Stojadinović, B. Münch, L. Suarez, B. Fumey, H. Hagendorfer, R. Brönnimann, P. Modregger, M. Gorbar, U. F. Vogt, A. Züttel, F. La Mantia, R. Wepf, and B. Grobéty. Three-dimensional pore structure and ion conductivity of porous ceramic diaphragms. *AIChE Journal*, 59:1446–1457, 2013.

[55] M. Doyle. Modeling of galvanostatic charge and discharge of the lithium/polymer/insertion cell. *Journal of The Electrochemical Society*, 140: 1526, 1993.

[56] M. Doyle and J. Newman. The use of mathematical modeling in the design of lithium/polymer battery systems. *Electrochimica Acta*, 40:2191–2196, 1995.

[57] K. Schladitz, J. Ohser, and W. Nagel. Measuring intrinsic volumes in digital 3D images. In A. Kuba, L. Nyúl, and K. Palágyi, editors, *13th International Conference on Discrete Geometry for Computer Imagery*, pages 247–258. Springer, 2007.

[58] B. Prifling, M. Röding, P. Townsend, M. Neumann, and V. Schmidt. Large-scale statistical learning for mass transport prediction in porous materials using 90,000 artificially generated microstructures. *Frontiers in Materials*, 8:786502, 2021.

[59] M. F. Lagadec, R. Zahn, and V. Wood. Characterization and performance evaluation of lithium-ion battery separators. *Nature Energy*, 4:16–25, 2019.

[60] J. Le Houx, M. Osenberg, M. Neumann, J. R. Binder, V. Schmidt, I. Manke, T. Carraro, and D. Kramer. Effect of tomography resolution on calculation of microstructural properties for lithium ion porous electrodes. *ECS Transactions*, 97:255, 2020.

[61] A. M. Colclasure, A. R. Dunlop, S. E. Trask, B. J. Polzin, A. N. Jansen, and K. Smith. Requirements for enabling extreme fast charging of high energy density Li-ion cells while avoiding lithium plating. *Journal of The Electrochemical Society*, 166:A1412–A1424, 2019.

[62] J. Laurencin, R. Quey, G. Delette, H. Suhonen, P. Cloetens, and P. Bleuet. Characterisation of solid oxide fuel cell Ni–8YSZ substrate by synchrotron X-ray nano-tomography: from 3D reconstruction to microstructure quantification. *Journal of Power Sources*, 198:182–189, 2011.

[63] T. Kanit, S. Forest, I. Galliet, V. Mounoury, and D. Jeulin. Determination of the size of the representative volume element for random composites: statistical and numerical approach. *International Journal of Solids and Structures*, 40:3647–3679, 2002.

[64] L. Holzer, D. Wiedenmann, B. Münch, L. Keller, M. Prestat, P. Gasser, I. Robertson, and B. Grobéty. The influence of constrictivity on the effective transport properties of porous layers in electrolysis and fuel cells. *Journal of Materials Science*, 48:2934–2952, 2013.

[65] A. Vadakkepatt, B. Trembacki, S. R. Mathur, and J. Y. Murthy. Bruggeman's exponents for effective thermal conductivity of lithium-ion battery electrodes. *Journal of The Electrochemical Society*, 163:A119, 2015.

[66] T. H. Cormen, C. E. Leiserson, R. L. Rivest, and C. Stein. *Introduction to Algorithms*. MIT Press, 2022.

[67] L. D. Gelb and K. Gubbins. Pore size distributions in porous glasses: A computer simulation study. *Langmuir*, 15:305–308, 1999.

[68] M. Neumann, C. Hirsch, J. Staněk, V. Beneš, and V. Schmidt. Estimation of geodesic tortuosity and constrictivity in stationary random closed sets. *Scandinavian Journal of Statistics*, 46:848–884, 2019.

[69] F. A. Dullien. *Porous Media: Fluid Transport and Pore Structure*. Academic Press, 1991.

[70] F. L. Usseglio-Viretta, A. Colclasure, A. N. Mistry, K. Claver, F. Pouraghajan, D. P. Finegan, T. M. Heenan, D. Abraham, P. P. Mukherjee, D. Wheeler, P. Shearing, S. J. Cooper, and K. Smith. Resolving the discrepancy in tortuosity factor estimation for Li-ion battery electrodes through micro-macro modeling and experiment. *Journal of The Electrochemical Society*, 165:A3403–A3426, 2018.

[71] J. Wang, J. K. Carson, M. F. North, and D. J. Cleland. A new approach to modelling the effective thermal conductivity of heterogeneous materials. *International Journal of Heat and Mass Transfer*, 49:3075–3083, 2005.